# A Study of the Interfacial Configuration of $Alq_3$ and Co Bilayer in Organic Spin Valves

A dissertation Submitted to the College of

Graduate Studies and Research

In Partial Fulfillment of the Requirements

For the Degree Master of Science

In the Department of Physics and Engineering Physics

University of Saskatchewan

Saskatoon

By

Muhammad Mahbub Husain

# PERMISSION TO USE

In presenting this thesis in partial fulfilment of the requirements for a Postgraduate degree from the University of Saskatchewan, I agree that the Libraries of this University may make it freely available for inspection. I further agree that permission for copying of this thesis in any manner, in whole or in part, for scholarly purposes may be granted by Dr. Gap Soo Chang or, in their absence, by the Head of the Department or the Dean of the College in which my thesis work was done. It is understood that any copying or publication or use of this thesis or parts thereof for financial gain shall not be allowed without my written permission. It is also understood that due recognition shall be given to me and to the University of Saskatchewan in any scholarly use which may be made of any material in my thesis.

Requests for permission to copy or to make other use of material in this thesis in whole or part should be addressed to:

Head of the Department

Physics and Engineering Physics

University of Saskatchewan

Room 163, 116 Science Place

Saskatoon, SK S7N 5E2

Canada

# ABSTRACT

The interfacial electronic structure of the organic material- tris(8-hydroxyquinolinato)aluminum ($Alq_3$) forming an interface with cobalt metal has been investigated in this research. The primary characterization method used in this research was near-edge X-ray absorption fine structure (NEXAFS) spectroscopy which probes the unoccupied molecular orbitals of a material. Density functional theory (DFT) calculations have also been employed to calculate the partial density of states (PDOS) of all constituent elements present in $Alq_3$ molecule. The DFT calculations helped to determine the molecular orbital structure of $Alq_3$ and to understand how the orbital structure is influenced by forming an interface with ferromagnetic Co layer. The experimental NEXAFS spectra measured in total fluorescence yield (TFY) showed that the lowest unoccupied molecular orbital (LUMO) and LUMO+1 states of $Alq_3$ were not affected by the presence of Co when Co is deposited onto $Alq_3$. On the other hand, a charge transfer between Co and $Alq_3$ led the loss or reduction of LUMO+2 state for a Co(top)/$Alq_3$ bilayer sample when compared to pristine $Alq_3$ reference sample (without Co deposition). This selective effect of Co on the orbital configuration of $Alq_3$ suggests that Co atoms diffuse into $Alq_3$ and interact with preferred sites in $Alq_3$. By comparing the spectral change in the experimental NEXAFS spectra to the calculated PDOS of $Alq_3$, the preferred interaction sites between Co and $Alq_3$ could be successfully determined. This work suggests that the spectroscopic approach using synchrotron-radiation X-ray spectroscopy can serve as a powerful means for studying the interfacial electronic structure between magnetic metals and organic semiconductors and can contribute to the research and development of high performance organic spintronics.

# ACKNOWLEDGMENTS

First and foremost, I am very glad to thank my supervisor, Dr. Gap Soo Chang, for all of his guidance, help, and support throughout my degree. His experience and patience with me has made this a truly enjoyable experience. Every meeting with him let me reunite my thinking and return to my work with better ideas and a sense of excitement about the discoveries just waiting to be made. I would also like to thank my coworkers who share my office, Paul, Jay and Robert who helped me many times doing experiments and understanding many things. They were always available to bounce ideas off of when I've been thinking in circles and need a jump start. I also would like to thank all of my friends, for whom, I was always made happy and fresh to go through much tough time.

I strongly and heartedly thank to my amazing loving parents, Dr. Muhammad Husain and Shamsun Nahar, who give everything I need and always encourage me in my study and help progress in my life.

Finally, my greatest honor and respect goes to the Almighty- *Allah*, who was and will be with me always, provides me everything necessary for me and gives me physical and mental health and peace regardless my bad or good deed. Without his help, it would never be possible to come to this level in my life.

# TABLE OF CONTENTS

Page

# LIST OF TABLES

# LIST OF FIGURES

# LIST OF ABBREVIATIONS

| | |
|---|---|
| NEXAFS | Near-edge X-ray Absorption Fine Structure |
| PVD | Physical Vapor Deposition |
| DFT | Density Functional Theory |
| MTJ | Magnetic Tunnel Junction |
| FM | Ferromagnetic |
| $Alq_3$ | Tris(8-hydroxyquinolinato)aluminum |
| DOS | Density of States |
| PDOS | Partial Density of States |
| TFY | Total Fluorescence Yield |
| TEY | Total Electron Yield |
| LUMO | Lowest Unoccupied Molecular Orbital |
| 3D | Three Dimensional |
| AFM | Antiferromagnetic |
| PM | Paramagnetic |
| CLS | Canadian Light Source |
| ALS | Advanced Light Source |
| BE | Binding Energy |
| SXF | Soft X-ray fluorescence |
| XAS | X-Ray Absorption Spectroscopy |
| XES | X-Ray Emission Spectroscopy |
| REIXS | Resonant inelastic X-ray scattering |
| MR | Magnetoresistance |
| AMR | Anisotropic Magnetoresistance |
| GMR | Giant Magnetoresistance |
| TMR | Tunneling Magnetoresistance |

| | |
|---|---|
| HMD | Hexamethyldisilazane |
| ODTS | Dichloromethyl-octadecylsilane |
| RRP3HT | Regioregular-poly(3-hexylthiophene) |
| LSMO | Lanthanum Strontium Manganite, $La_{1-x}Sr_xMnO_3$ |
| HK | Hohenberg-Kohn |
| KS | Kohn-Sham |
| LDA | Local Density Approximation |
| LSDA | Local Spin Density Approximation |
| GGA | Gradient Approximation |
| B3LYP | Becke Three-parameter Lee-Yang-Parr |
| FWHM | Full Width Half Maximum |
| MO | Molecular Orbital |
| LCAO | Linear Combinations of the Atomic Orbitals |
| SDD | Silicon Drift Detector |
| CVD | Chemical Vapor Deposition |
| AMDR | Advanced Materials/Devices Research |

# CHAPTER 1

# INTRODUCTION

Spin electronics or magneto-electronics, commonly referred to as spintronics, is a study based on the manipulation and control of the intrinsic spin in addition to charge of the electrons. Electrons' spins can be manipulated in electronic devices by applying an external magnetic field. Nowadays spintronics has garnered enormous interest from the materials science and engineering community because of its various potential uses such as developing low power consumption devices and also producing high speed and non-volatile memory modules by utilizing electrons' spin magnetic moment. Electron can be either "spin-up" or "spin-down", also referred to as 'majority' and 'minority' spins, which are used to the record binary 1 and 0 (on and off, respectively) in the digital electronic systems; hence data can be stored for very long time by preserving the spin magnetic moments in a material, in the absence of continuous supply of conventional charge current (electricity) in the spintronic memory devices. Other types of spintronic devices include spin transistors, giant magnetoresistance (GMR) heads (used in hard disk drives) and magnetic tunnel junction (MTJ) devices. Spintronics research has been done on both organic and inorganic materials. Recently, research on the use of organic materials in spintronics has become increasingly popular because these carbon-based molecular materials typically have a low spin-orbit interaction leading to long spin diffusion length as well as long spin relaxation time. Moreover, organic materials are generally inexpensive, flexible and environment-friendly, which also made them attractive and preferable for use in commercial applications.

The most basic structure of a spintronic device, e.g. the tri-layered spin valve, contains a ferromagnetic (FM) electrode for spin injection, a spin transport layer and a spin detection electrode which can also be an FM metal or half metal. The transport layer, referred to as space layer can be an antiferromagnetic (AFM) metal [1], paramagnetic (PM) metal [2], oxide insulator, or single or multilayered organic semiconductors. The research in this thesis is based on the organic material. Here, the interfacial electronic structure of an organic material forming an interface with a FM metal (cobalt in this case) has been investigated in order to understand the effect of the interfacial configuration of the organic/FM bilayer on the device performance of organic spin valves. Fig. 1.1 illustrates a schematic picture of a spin valve structure.

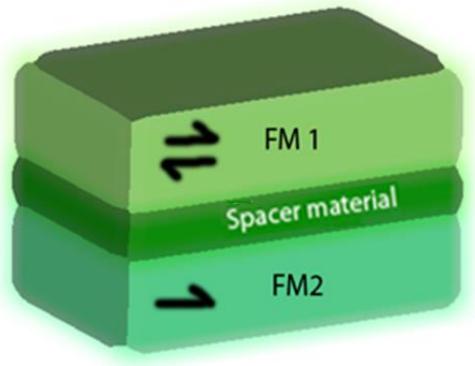


Figure 1.1: Schematic diagram of a vertical spin valve structure. The arrows indicate the magnetization direction associated with two ferromagnetic layers (FM1 and FM2).

As shown in Fig. 1.1, two different types of magnetic materials are used as electrodes, which are separated by a spacer material. The top electrode, FM1, is made of a soft magnetic material with low coercivity field ($H_c$) and the FM2 electrode is made of a hard magnetic material with high $H_c$. One can therefore switch the magnetization direction of FM1, leaving the

magnetization of FM2 fixed in one direction by applying an external magnetic field in the limit of $H_c$ of FM2. In organic spin valves, the ferromagnetic half metal (e.g., $La_{1-x}Sr_xMnO_3$), which is conducting for spin-majority electrons and insulating for spin-minority electrons, is widely used as one electrode. When an electric potential is applied between two electrodes under external magnetic field, spin-polarized carriers are injected from FM1 and transported to the other electrode FM2 through the spacer layer. The carrier transfer can be made by either the tunneling process or the hopping process depending on the thickness of the spacer layer.

The organic material used in this research is tris(8-hydroxyquinolinato)aluminum ($Alq_3$). $Alq_3$ is a well-known *n*-type π-conjugated semiconductor, which has been actively used as an electron-transport material in organic light emitting devices [3]. This non-planar molecule contains three 8-hydroxyquinoline ligands, which are connected in unequal angles with the center Al atom (see Fig. 1.2). Due to this three dimensional molecular structure, the surface and crystal structure of this material is highly disordered. The chemical structures of the $Alq_3$ molecule and 8-hydroxyquinoline ligand are shown in Fig. 1.2.

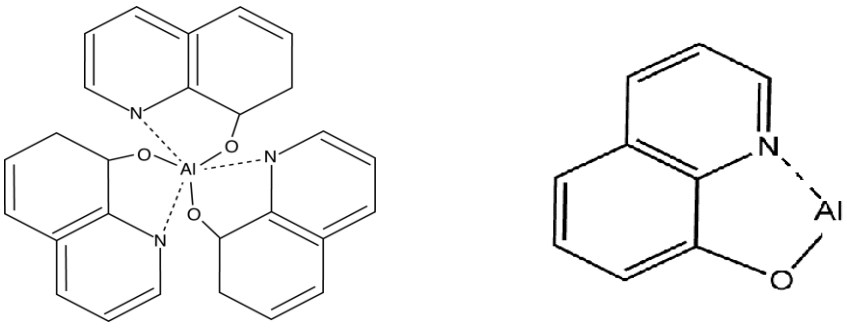


(A) (B)

Figure 1.2: Chemical structure of (A) $Alq_3$ molecule and (B) single 8-hydroxyquinoline ligand.

This study includes how deposition of the Co onto $Alq_3$ can affect the interface of the Co and $Alq_3$ material. It was reported that Co can diffuse into $Alq_3$ and result in the rough surface between the two layers. Since this Co diffusion may cause deterioration in the spin transport performance of an organic spin valve [4], it has been investigated here how this Co diffusion into the organic spacer layer possibly can affect the electronic structure of $Alq_3$. The experiments were performed on the bilayer sample architectures, $Co/Alq_3$. The samples were fabricated on an Si (100) wafer with thermally grown $SiO_2$ layer (100 nm). The interfacial electronic structure of $Co/Alq_3$ bilayered samples was measured using NEXAFS spectroscopy at Canadian Light Source (CLS) and Advanced Light Source (ALS), Berkeley, CA, USA. The PDOS of $Alq_3$ was calculated employing density functional theory (DFT) and was compared with the experimental NEXAFS spectra.

Including this introduction, the dissertation consists of six chapters. The background of this study which drives the idea of selecting this research on specific materials and experimental techniques is given in the "Background" (Chapter 2). Other than this, the theoretical background of molecular orbital structure of organic materials and density functional theory are explained in the "Theory of molecular orbital structure" (Chapter 3). The experimental procedures which include the sample preparation and NEXAFS measurements are described in the "Experimental description" (Chapter 4). The data analysis of C and Co NEXAFS spectra for $Co/Alq_3$ bilayers are discussed in the "Results and discussion" (Chapter 5). Finally, the summary of this research is presented in the "Summary and Future Work" (Chapters 6).

# CHAPTER 2

# BACKGROUND

In this chapter a summary on previous research on spintronic devices based on organic materials and issues for the development of high performance organic spin valves is presented. Starting from the magnetoresistance (MR) effect, this section will discuss how other groups attributed MR effects to the intrinsic properties of the organic spacer material in their devices as well as effects due to change of temperature, thickness and external magnetic field.

## 2.1 Magnetoresistance

Magnetoresistance, which means a change in the electrical resistance due to an external magnetic field, is an intrinsic property of a material, and can sometimes be observed in ultrathin multilayered structures. The MR effect was first discovered by William Thompson in 1851. He measured a change in the electrical resistance of Fe and Ni up to 5 % when he changed an angle between the current and the external magnetic field [5]. This effect is referred to as anisotropic magnetoresistance (AMR). More recently, much larger MR was obtained from metallic multilayered films. In 1988, Albert Fert and Peter Grünberg independently discovered a giant magnetoresistance (GMR) in [Fe(30 Å)/Cr(9 Å)]$_{40}$ multilayers and Fe(250 Å)/Cr(10 Å)/Fe(250 Å) sandwich layers, respectively [6,7]. When an external magnetic field was applied along the in-plane direction, the resistance at 4.2 K was reduced by almost 50 % with respect to the value under zero magnetic field. In addition to the importance of this discovery of GMR for spintronics, their pioneering work of nanometer fabrication is also recognized as the beginning of nanotechnology. Another type of MR effect was observed in a magnetic tunnel junction (MTJ) which consists of two magnetic layers separated by a thin insulating space layer. This effect is

referred to as tunneling magnetoresistance (TMR) because spin-polarized electron transport between two magnetic electrodes is mediated by a quantum mechanical tunneling process. The TMR effect is known as a key property in the development of magnetic random-access memory (MRAM) devices these days. The TMR can be controlled by a relative magnetization alignment between two magnetic electrodes (see Fig. 2.1). The TMR effect was first discovered by Julliere [8] in 1975. He observed a change of resistance around 14 % in Fe/GeO/Co MTJ structure at 4.2 K and explained the TMR effect with the spin polarizations of two magnetic electrodes. According to the Julliere model, the TMR magnitude can be defined as [8]:

$$TMR = \frac{R_{AP} - R_P}{R_P} = \frac{2P_{FM1}P_{FM2}}{1 - P_{FM1}P_{FM2}} \tag{2.1}$$

where $R_{AP}$ ($R_P$) is the electrical resistance for antiparallel (parallel) alignment of the magnetization between two magnetic electrodes. The $P_{FM1}$ ($P_{FM2}$) represents the spin polarization of a magnetic electrode FM1 (FM2), which is expressed as:

$$P = \frac{N^{\uparrow}(E_F) - N^{\downarrow}(E_F)}{N^{\uparrow}(E_F) + N^{\downarrow}(E_F)} \tag{2.2}$$

where N($E_F$) is the spin-dependent density of states (DOS) of a magnetic electrode at the Fermi level. Julliere's small TMR value did not bring much attention at the time of discovery, but later a TMR effect of 604 % at room temperature and 1144 % at 5 K was reported in the CoFeB/MgO/CoFeB MTJ devices by Ikeda *et al*[9].

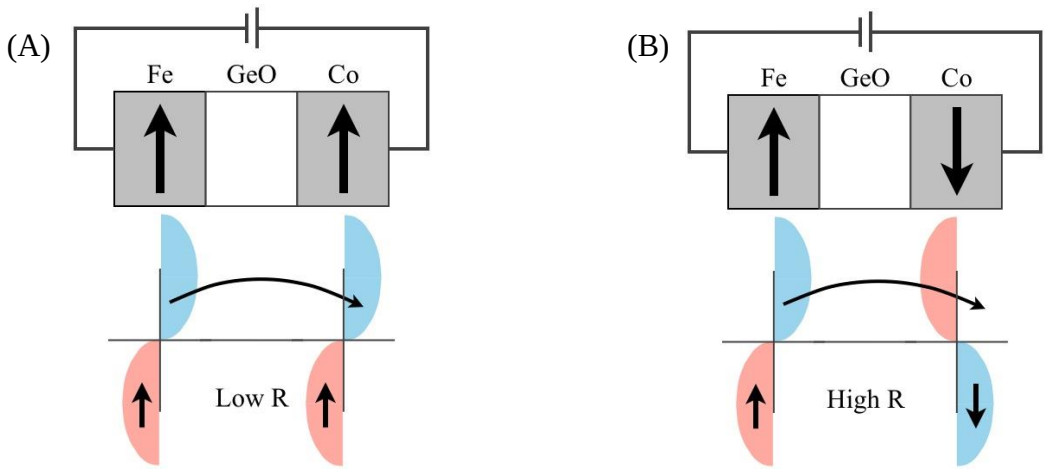


Figure 2.1: Schematic of TMR effect of Fe/GeO/Co MTJ for (A) parallel magnetization alignment (low resistance) and (B) anti-parallel alignment (high resistance).

## 2.2 Magnetoresistance in Organic-based Spin Valves

In addition to inorganic oxides, organic semiconductors have been more recently investigated as a promising space material for spin-valve devices due to their low spin-orbit coupling and long spin-relaxation time in excess of 10 μs [10,11]. This means that the spin-polarized carriers injected into the organic spacer can be preserved for a long time and distance compared to transition metal oxides. The first MR effect from an organic-based spin valve was observed by Dediu *et al*. [12] in 2002. They used sexithiophene ($T_6$) as an organic spacer material. Also, lanthanum strontium manganite ($La_{1-x}Sr_xMnO_3$, LSMO) was used as a magnetic electrode because of its a ferromagnetic half metallic property (conductor for majority or spin-up electrons and insulator for minority or spin-down electrons) and also it has nearly 100 % spin polarization at a Curie temperature of 270 K and therefore can be an ideal material for efficient spin injection/detection [13]. Using the LSMO/$T_6$/LSMO structure, MR of only roughly 10~25 % could be obtained. The intense research on organic spin valves was later triggered by the achievement of a high GMR value in a LSMO/$Alq_3$/Co structure by Xiong *et al.*[14]. From the

LSMO (100 nm)/$Alq_3$ (130 nm)/Co (3.5 nm) spin-valve structure, they obtained GMR of 40 % at 11 K. On the other hand, they were unable to detect any MR effect for a thickness of $Alq_3$ below 100 nm. They suspected that a disappearance of the MR effect might be due to Co diffusion into the $Alq_3$ layer, leaving no pure $Alq_3$ bulk state. From this fact, they suggested that even for a thickness of $Alq_3$ higher than 100 nm, the Co/$Alq_3$ interface might have a Co-$Alq_3$ mixed sublayer, called a defected or ill-defined sublayer. Riminucci *et al*. fabricated LSMO/$Alq_3$ (200 nm)/Co spin valves with a tunnel barrier of 2 nm $Al_2O_3$ (or LiF) between $Alq_3$ and Co in order to prevent the diffusion of Co into $Alq_3$ and thus make a sharp Co/$Alq_3$ interface [15]. They, however, observed very low MR values of about 2 % at 100 K and the MR values were not enhanced by the presence of a thin tunnel barrier. The same approach was also made by Dediu *et al*. [16], and using the Co/$Al_2O_3$ (1-2 nm)/$Alq_3$ (200 nm)/LSMO spin-valves, they could observe the MR effect at room temperature, although it was a mere 0.15 %.

It should also be noted that the MR values obtained in organic spin valves mentioned above, were negative; that is, the MR became lower for antiparallel alignment of magnetization between LSMO and Co electrodes than for parallel alignment. This negative MR (or inverse MR) is unusual as conventional inorganic spin valves show positive MR (i.e., higher MR for antiparallel alignment of the magnetization than parallel alignment) (see Fig. 2.1). Xiong group attributed this inverse MR effect to the negative spin polarization of the Co *d*-band, implying the smaller density of states (DOS) of the spin-majority sub-band at the Fermi level than that of the spin-minority sub-band [14]. This negative spin polarization of the Co electrode ($P_{Co} < 0$) leads to the negative TMR value obtained from the Julliere model (see Eq. 2.1). However, they could not provide a detailed physical explanation and the mechanism of spin injection/transport in

organic spin valves has not been fully understood. It yet remains one of the main challenges in organic spintronics technology.

Following these findings, several contradicting results such as positive a MR effect or absence of the MR effect in organic spin valves were also reported by several research groups [17, 18, 19]. Santos *et. al.* reported a large positive TMR effect at room temperature in $Co/Al_2O_3/Alq_3/NiFe$ spin valves [17]. The Majumdar group used regioregular-poly(3-hexylthiophene) (RRP3HT) as an organic spacer material in Co/RRP3HT (100 nm)/Co spin valves and obtained 1.5 % of MR at room temperature [18]. In addition, when they spin-coated a monolayer of hexamethyldisilazane (HMD) or dichloromethyl-octadecylsilane (ODTS) polymeric insulator prior to deposition of the RRP3HT onto LSMO, the MR values were drastically reduced by completely damaging the spin injection into RRP3HT.

Furthermore, Jiang *et al.* reported negligible or no MR effect in the $Fe/Alq_3/Co$ spin valves [19]. When a 25 to 150 nm thick $Alq_3$ spacer layer was inserted between Co and Fe layers, they obtained no measurable MR. It was also observed that $Fe/Alq_3/Co$ spin valves transport hole carriers only and this hole-only transport in $Alq_3$ is injection-limited although $Alq_3$ is known to be an *n*-type semiconductor [20]. This absence of MR in their spin valves with a thick organic layer supports that the MR effect in organic spin valves is based on the tunneling process and the large conductivity mismatch at ferromagnetic metal-organic semiconductor interfaces significantly prevents efficient spin injection across the interface.

As is obvious from the above discussion, spin injection and transport in organic spin valves have not been fully understood yet due to the lack of consistency in the sign of the MR effect. The overall results reflect that an interfacial configuration between the organic spacer

layer and top magnetic electrode is strongly related with the sign and magnitude of the MR values. Therefore, an extensive investigation on the metal-organic interface is highly desirable for better understanding the spin transport mechanism in spintronic devices.

# CHAPTER 3

# THEORY OF MOLECULAR ORBITAL STRUCTURE

In the present study, synchrotron-radiation X-ray spectroscopy is employed as a major characterization tool to investigate the interfacial configuration of the $Alq_3$/Co bilayered system. The molecular orbital calculations of constituent atoms in the organic spacer material will help to interpret experimental NEXAFS spectra which selectively probe the density of states of a target element. For calculation of molecular orbital states, density functional theory has been used in present study. In this chapter, details about molecular orbital theory are given and the basic theory for calculations of molecular orbital states is described.

## 3.1 Molecular Orbital Theory

Doing research on the electronic structure of organic π-conjugated materials requires a good understanding of the theory behind the configuration of molecular orbitals.In a molecular system, the atoms are bonded in a certain way depending on their electronic configurations and create energy states, different from individual atoms, which depend on the type of the atomic/molecular bonding. Molecular orbital (MO) theory provides a basic concept which approximates how two atoms can be bonded together. When two atoms come close to each other, the wavefunctions of each atom overlap and form a combined wavefunction of a two-atom system. In MO theory, the molecular wavefunction is considered to be constructed by linear combinations of the atomic orbitals (LCAO). The MO is said a combination of σ and π bonding orbitals, and σ* and π* antibonding orbitals. For a better understanding of atomic orbital structure and the formation of the MO according to this theory, a description is given as follows.

First let us consider an atom with low atomic number (Z), e.g C as it is relevant to this research. The electronic configuration of the C atom ($Z = 6$) is $1s^2 2s^2 2p^2$ i.e. it possesses *s* and *p* orbital in its configuration. Due to different orbital angular momentum quantum numbers ($l$) the wavefunction of *s* electron ($l = 0$) is only radial-dependent while that of *p* electron ($l = 1$) must be described by a radial function as well as a spherical harmonic. This results different shapes for *s* and *p* orbitals as shown in Fig. 3.1.


Figure 3.1: Shape of the (A) 1*s* orbital and (B) 2*p* ($p_x$, $p_y$ or $p_z$) orbital. In the 2*p* orbital structure, different coloring indicates the opposite phases of the orbital.

The *p* orbital is split along three directions and has $p_x$, $p_y$ and $p_z$ components. In Fig. 3.1, we see that the *p* orbital has two oval shapes of different phases together, which are called lobes. These lobes determine whether an orbital has antibonding character or bonding character. Two lobes of the symmetric phase form a bonding orbital and two antisymmetric lobes form antisymmetric bonding orbitals. The antibonding orbital contains a node between two nuclei. Fig. 3.2 depicts the formation of bonding and antibonding orbitals from a hybridization of two $p_z$ orbitals. In addition, depending on the type of the molecule, the C atoms can also be hybridized in different ways, such as *sp*, $sp^2$ or $sp^3$ bonding.

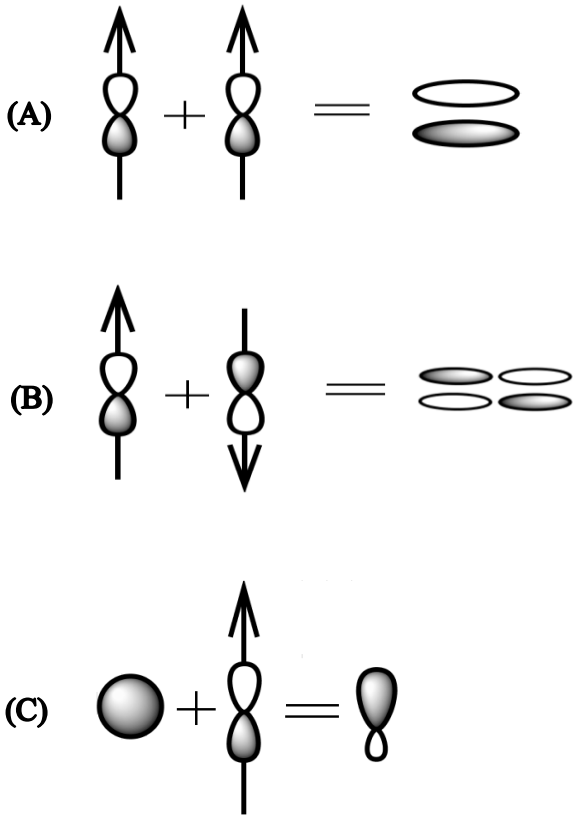


Figure 3.2: A schematic diagram of the two $p_z$ orbitals of two C atoms form (A) π-bonding, (B) π*-antibonding orbitals and (C) shape of the $sp^2$ orbital.

Now let us take ethylene ($C_2H_4$) as an example of a C-based molecular system. The electronic configuration for a C atom in one of these hybridizations is $1s^2 2s^1 2p_x^1 2p_y^1 2p_z^1$. For an ethylene molecule, C atoms form $sp^2$ hybridization (see Fig. 3.2C) in which one 2*s* and two other 2*p* orbitals are mixed together, and in this case one *p* orbital remains untouched. A total of three $sp^2$ orbitals are formed in this way. Then one $sp^2$ orbital from one C atom forms a σ-bond by connecting with another $sp^2$ orbital of its C neighbor atom along the same direction. The untouched *p* orbitals of these two C atoms then make a π-bond and construct a double bond between two C atoms. The other two $sp^2$ orbitals connect with the *s*-orbital of H and form a σ-bond between C and H.

### 3.2 Density Functional Theory

Density functional theory (DFT) is a widely used technique for modeling of the electronic structure of many body systems at the ground state. DFT is based on quantum mechanical calculations to solve the Schrödinger equation in terms of electron density and thus compute the ground state density of states (DOS) of a material. DFT is founded on the Kohn-Sham equations [21] which are useful to acquire the ground state energy with the electrons' density in an interacting many-electron system. First of all, consider an exact Hamiltonian of a stationary system, in which the kinetic energy of the electrons, coulomb interactions of electron-electron, electron-nuclei and nuclei-nuclei are present. For this stationary system, Born-Oppenheimer approximation can be made in order to make the Hamiltonian simple [22], considering that the kinetic energy of the nuclei turned to zero and the coulomb interaction of the nuclei-nuclei can be thought as constant. In such a case, the Hamiltonian of that system can be expressed by three terms:

$$\widehat{H} = \hat{T} + \hat{V} + \widehat{W} \tag{3.1}$$

where $\hat{T}$, $\hat{V}$ and $\widehat{W}$ in the above equations represents of the kinetic energy operator, the potential operator for interaction with external potential and the coulomb interaction potential operator [23]. This external potential is added as it is considered that the electrons can move in a potential in an electronic system [24] and hence this potential is the potential energy of the electron in the potential of the nuclei of the system [22]. Also, for all many electron systems, both the kinetic energy and the coulomb interaction of the electron are totally independent and the only part which we have to consider for getting information about the system is $\hat{V}$. To solve the Schrödinger equation for the system described above, Hohenberg and Kohn established two

theorems, which make the solution simpler [25]. The first theorem says that the ground state expectation value for any observable, say $\hat{O}$, can be represented as a functional of the ground state electron density ($\rho$) as given in Eq. 3.2; and secondly, if the observable is the Hamiltonian of the system, then the ground state energy, $E_{ext}$, for the system with a non-degenerate ground state and an external potential, can be written as in Eq. 3.3.

$$O(\rho) = \langle\psi|\hat{O}|\psi\rangle \tag{3.2}$$

$$E_{ext}(\rho) = \langle\psi|\hat{T} + \widehat{W}|\psi\rangle + \langle\psi|\hat{V}|\psi\rangle \tag{3.3}$$

or,
$$E_{ext}(\rho) = F_{HK} + \langle\Psi|\hat{V}|\Psi\rangle \tag{3.4}$$

$$\text{where, } F_{HK} = \langle\psi|\hat{T} + \widehat{W}|\psi\rangle \tag{3.5}$$

where $F_{HK}$ is defined as the Hohenberg and Kohn (HK) functional [21]. The HK theorems explain that Eq. 3.3 represents the total ground state energy of the system, i.e., the ground state energy can be obtained from the energy of the external potential when the Hamiltonian of the system is a functional of the ground state density. This suggests that any information of the observable can be written as a functional of the density and according to the HK theorem the electron density contains the whole information of the wave function. Therefore, only knowing the electron density can retrieve the information of a system's Hamiltonian. A more approximate solution can be achieved using the Kohn-Sham (KS) equation where one can rewrite the HK functional in the KS version of the Hamiltonian, $\widehat{H}_{KS}$ [26]. The KS theorem considers an inhomogeneous non-interacting electron system and approximates the kinetic energy and coulomb interaction potential to calculate the ground state energy of an inhomogeneous interacting electron system. Kohn-Sham approximated that the total energy can be represented by

separating the coulomb interaction potential to the exchange correlation and Hartree potential. The $F_{HK}$ functional can be rewritten as:

$$F_{HK} = T_o(\rho) + V_H(\rho) + V_{xc}(\rho) \tag{3.6}$$

In the above equation, $T_o$, $V_H$ and $V_{xc}$ represent the kinetic energy functional for non-interacting system, the potential for Hartree contribution and the exchange correlation potential, respectively. Now using Eq. 3.6, one can rewrite Eq. 3.4 as:

$$E_{ext}(\rho) = T_o(\rho) + V_H(\rho) + V_{xc}(\rho) + \langle\psi|\hat{V}|\Psi\rangle \tag{3.7}$$

Using the Schrödinger equation, $\hat{H}|\psi\rangle = E|\psi\rangle$ and Eq. 3.1, one can find the Hamiltonian of a system, which is called the Kohn-Sham Hamiltonian, $\hat{H}_{KS}$:

$$\hat{H}_{KS} = \hat{T}_o + \hat{V}_H + \hat{V}_{xc} + \hat{V} \tag{3.8}$$

The exchange correlation functional $\hat{V}_{xc}$ in the above equation is a functional derivative:

$$\hat{V}_{xc} = \frac{d}{d\rho} V_{xc}(\rho) \tag{3.9}$$

Finally, from the Kohn-Sham approximation, where the system is considered as homogenous electron gas, the exact ground state density $\rho(\vec{r})$ and $\hat{H}_{KS}$ for an N-electron system can then be expressed as [22]:

$$\rho(\vec{r}) = \sum_{i=1}^{N} \emptyset_i(\vec{r})^* \emptyset_i(\vec{r}) \tag{3.10}$$

$$\hat{H}_{KS}\emptyset_i = \epsilon_i \emptyset_i \tag{3.11}$$

where $\emptyset_i$ represent the single particle wavefunction.

In the above discussion the exchange correlation functional is not known yet and hence there needs to be another approximation, such as the local density approximation (LDA) or the local spin density approximation (LSDA) for spin polarized form [27]. In this approximation, it is assumed that the material is a collection of very small volumes and all volumes have identical electron density as the original material. All volumes are then thought to contribute equal amount of exchange correlation energy which is in total the exchange correlation energy of the total volume. A further approximation method was also developed from the LDA which is called called generalized gradient approximation (GGA), where the density of the neighboring volume was also considered. The exchange correlation functional according to LSDA and GGA are as below:

$$E_{xc}^{LSDA}[\rho_{\downarrow}(\vec{r}),\rho_{\uparrow}(\vec{r})] = \int \rho(\vec{r}) e_{xc}\,(\rho_{\downarrow}(\vec{r}),\rho_{\uparrow}(\vec{r}))d^3r \tag{3.12}$$

$$E_{xc}^{GGA}[\rho_{\downarrow}(\vec{r}),\rho_{\uparrow}(\vec{r})] = \int \rho(\vec{r}) e_{xc}(\,\rho_{\downarrow}(\vec{r}),\rho_{\uparrow}(\vec{r}),\nabla(\rho_{\downarrow}(\vec{r}),\nabla\,\rho_{\uparrow}(\vec{r})))d^3r \tag{3.13}$$

In the Eq. 3.12 and 3.13, $e_{xc}$ is the exchange correlation energy for each electron. The up and down arrow represent the spin state of the electrons.

In this research *Gaussian03* program package was used for calculating the molecular orbital states of constituent atoms in an $Alq_3$ molecule. This program uses the exchange correlation functional and basis sets for both structural and geometrical optimization and the energy calculations. For the molecular orbital calculations of the $Alq_3$, Becke three-parameter Lee-Yang-Parr (B3LYP) functional and 6-31G basis set were used [28, 29]. The 6-31G basis set can be used for molecules from $1s^2$ to $4s^2$, $4p^6$. The B3LYP exchange correlation functional which is expressed as [30]:

$$E_{xc}^{B3LYP} = E_{xc}^{LSDA} + 0.2(E_x^{HF} - E_x^{LSDA}) + 0.72(E_x^{GGA} - E_x^{LSDA}) + 0.81(E_C^{GGA} - E_C^{LSDA}) \qquad (3.14)$$

where, $E_c$ and $E_x$ are the correlation and exchange functional and $E_x^{HF}$ is the exchange functional by Hartree-Fock approximation- an approximation method for calculating the total energy of a many electron system by considering individual wavefunctions of the electrons in that system. Thus it is seen from the Eq. 3.14 that the B3LYP exchange correlation function is a hybrid functional which contains the exchange and correlation functional by three approximation methods.

# CHAPTER 4

# EXPERIMENTAL DESCRIPTION

## 4.1 Near Edge X-Ray Absorption Fine Structure Spectroscopy

X-ray absorption spectroscopy is a powerful tool for studying the electronic structure of a material and probing its physicochemical properties, especially when it is combined with extremely bright synchrotron radiation. In this technique, the sample which needs to be analyzed may be hit by X-rays in a definite range from only a few eV up to hundreds of keV, depending on the atomic properties of the system. The system in this research is an organic semiconductor material i.e. based mainly on C atoms, so soft X-rays are used to determine the electronic properties here.

The valence levels of a system are denoted as K, L, M shell in condensed matter physics and chemistry notation. The binding energy (BE) is defined as the energy necessary to remove or ionize an electron from core level to the vacuum level or continuum. By absorbing the photon energy of radiation, a core level electron can be excited and hence can transfer its energy to another higher level electron or can emit a photon and return to the ground state energy levels. If the energy of the radiation is the same as the binding energy or ionization potential of the electron, an electron can be removed or excited to a higher energy level in the system.

### 4.1.1 Synchrotron Radiation

The NEXAFS measurement requires a synchrotron facility that can generate a highly controlled monochromatic photon beam. The research in this thesis is based on the Canadian

Light Source (CLS) at the University of Saskatchewan in Saskatoon and the Advanced Light Source (ALS) at Lawrence Berkeley National Laboratory in California, USA. Both of these laboratories have many facilities for spectroscopic experiment including NEXAFS. The beamlines used in this research for NEXAFS are the Spherical Grating Monochromator (SGM) beamline [31] at the CLS and Soft X-ray fluorescence (SXF) endstation at Beam line 8.0.1. at the ALS [32]. The SGM is an undulator beamline that can produce photons precisely tunable from 250 to 2000 eV which is ideal for measurement of light elements such as C, N and O [33]. The SXF beamline has an energy range between 80 to 1250 eV and is optimized for X-ray emission spectroscopy (XES) and Resonant inelastic X-ray scattering (RIXS) spectroscopy measurement [34], but can also perform NEXAFS.

In the synchrotron facility, light for the experiment is produced by accelerating electrons at a very high speed. These facilities generally contain four basic parts in their structure- linear accelerator, booster, storage ring and end stations (beamlines). The electrons are initially fed through the linear accelerator stage, and further accelerated using radio frequency waves in the booster ring close to the speed of light. Then these high energy accelerated electrons are transferred to the storage ring where they may circulate for several hours with a stable energy. This beam is controlled using magnets to fix it travelling in a circular path. The magnets also direct the beam to enter the required end stations where experiments are performed. As this research is concerned to the metal-organic interface analysis, therefore, only basic details of the measurement technique will be given here. In the X-ray spectroscopic measurement, the information is collected in two ways. When the monochromatic photons hit the sample, the core level electrons are excited to the higher energy levels as said before. This excited electron must decay to lower energy levels by emitting energy as photons or by transferring energy to other

neighboring electrons in that higher level. Those electrons that absorb the energy can then leave sample as Auger electrons and produce a charge on the sample measured as current, called total electron yield (TEY). Similarly emitted photons may be gathered as fluorescence,which is called total florescence yield (TFY) in the experiment. Both of these techniques provide a measurement of the total absorption cross section of the sample. The basic detail of the auger effect is discussed below.

### 4.1.2 Auger Effect

The X-ray absorption measurement is basically based on an internal mechanism or, effect of electron transition in atom which is called Auger effect. When a core level electron is excited to a higher level it creates an empty space hole in the core level. Therefore an electron from higher level can fill this hole and emits a specific amount of energy as a photon. These photons can leave the sample as fluorescence or can transfer energy to the nearer electrons which can then leave the sample. The fluorescence coming out of the sample by this process can be measured which is the TFY measurement. The final electron is called the auger electron. If the first excited electron is from the K-shell and the transition of second and the emission of third electrons are from L-subshell, this auger process is denoted as a KLL Auger process. A simple picture of the Auger electron effect is shown in Fig. 4.1. In this figure, an electron from the core level (K shell) is excited after absorbing the external energy (e.g. Coming photon energy from X-ray) and excited to the higher level leaving a hole (yellow colored) in the K shell. This core hole is then filled by another electron from $L_1$ subshell. While coming to the lower energy K level from higher L level, this electron releases the extra energy which is transferred to an electron in the $L_{2,3}$ subshell. The last electron is excited again and can continue the same process, or can be

excited enough to go to the continuum states of that atom. The Auger process described here is a KLL process where the auger electron comes from the L subshell.

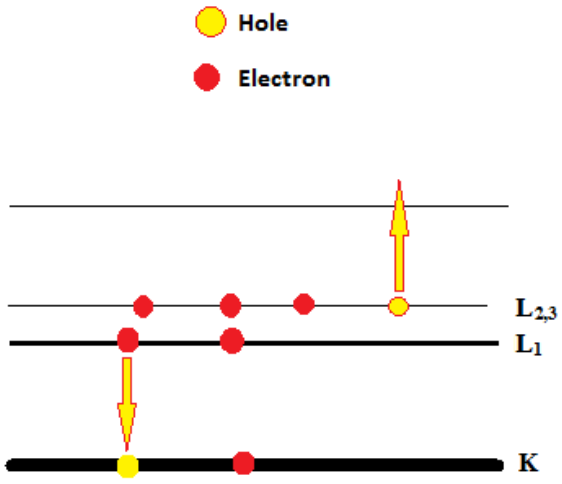


Figure 4.1: Schematic or Auger process showing the electron de-excitation from $L_1$ to K and an electron emitted from $L_{2,3}$. This is a $KL_1L_{2,3}$ process where two holes created in the L shell.

### 4.2 Physical Vapor Deposition

For the preparation of metal/organic semiconductor bilayered thin films, physical vapor deposition (PVD) was employed which is available in the Advanced Materials/Devices Research (AMDR) laboratory of the Department of Physics and Engineering Physics. A thin film of organic semiconductor can also be prepared by a solution-processed spin coating technique. However, it is not applicable to $Alq_3$ due to its low solubility to common organic solvents [35]. Furthermore, the PVD system in AMDR laboratory is equipped with low temperature evaporator furnaces for organic materials and high temperature evaporator for metals. Therefore, thin films of Co and $Alq_3$ can be fabricated in situ without breaking vacuum. Fig. 4.2 shows the PVD equipment is used for the sample preparation in this research.

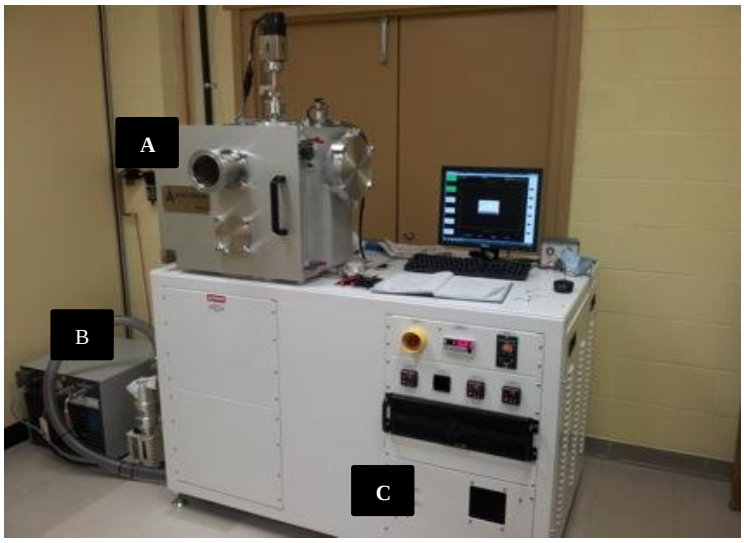


Figure 4.2: A picture of the PVD equipment used for the sample preparation for this research; (A) deposition chamber, (B) vacuum pumps (cryo-pump and rotary-vane pump) and (c) control panel.

For deposition of organic materials at low temperature (below 800 $^{o}$C), alumina crucibles are used while tungsten boats are used for deposition of transition metals at high temperature (over 1000 $^{o}$C). Several steps should be taken when preparing a thin film using the PVD technique. The source materials to be deposited are first placed in each crucible and the substrate is mounted upside down on the disk-type sample holder (see Fig. 4.2). Then the chamber is pumped out to a base pressure of $1\times10^{-7}$ torr using a rotary-vane roughing pump and cryo-pump for high vacuum. When the deposition rate for a material is stabilized, the shutter located in front of the sample holder can open and the material deposition starts.

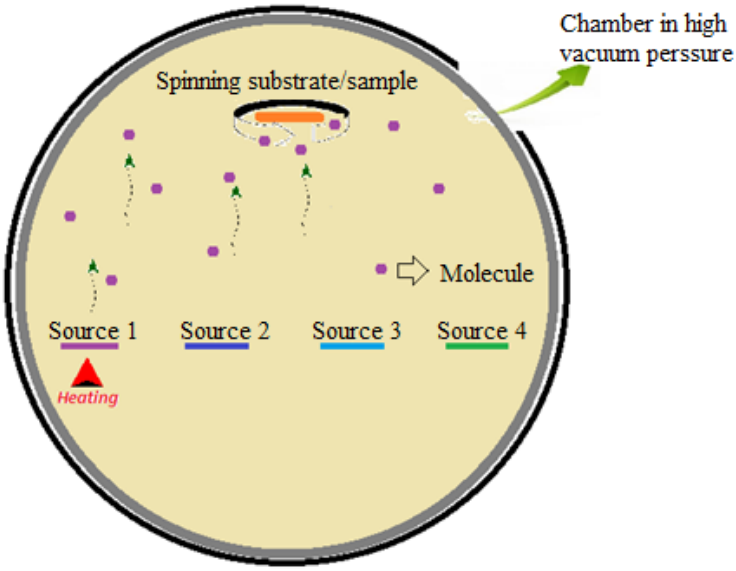


Figure 4.3: A schematic diagram of a PVD system, containing four separate sources. The sources are deposited onto the sample or the substrate which is placed on a plate upside down over the sources, on top of the chamber inside.

During film deposition, the deposition rate and film thickness can be monitored by a quartz crystal microbalance. Once the film thickness reaches a preset value, the shutter is closed automatically to prevent further deposition onto the sample.

### 4.3 Sample Preparation

In present study, 99.99 % pure $Alq_3$ which was purchased from Sigma-Aldrich. Si (100) wafer with thermally oxidized $SiO_2$ was used as a substrate (University Wafer Inc.). Co(top)/$Alq_3$ and $Alq_3$(top)/Co bilayered samples have been prepared by switching the deposition sequence of Co and $Alq_3$. For the Co(top)/$Alq_3$ sample, 150 nm thick $Alq_3$ film was deposited onto $SiO_2$ substrate at a deposition rate of 0.15 nm per second and 8 nm thick Co film was deposited at much lower deposition rate of 0.06 nm per second. The $Alq_3$(top)/Co bilayered sample with the

same $Alq_3$ and Co thicknesses as Co(top)/$Alq_3$ sample was prepared at the same deposition rates. In addition to the bilayered thin films, Co and Alq3 single layers were also prepared as reference samples for spectroscopic measurements at CLS and ALS.

# CHAPTER 5

# RESULTS AND DISCUSSION

## 5.1 Molecular Structure Analysis:

Before simulation of the molecular orbitals of $Alq_3$, its molecular geometry was optimized using the *Gaussian03*. Fig. 5.1 shows the molecular structure of $Alq_3$ from two different angles after structure optimization. As an $Alq_3$ molecule is comprised of a total of 52 atoms of 5 different elements (1 Al atom, 3 O atoms, 3 N atoms, 18 H atoms, and 27 C atoms), *Gaussian03* assigns the atoms with numbers automatically. The numbering of all constituent atoms is also presented in Fig. 5.1 and Table 5.1. Note that the same numbering is used to represent calculated partial density of states (PDOS) spectra shown in the following figures and discussion. As will be discussed later, the spectroscopic and theoretical analysis has focused on the PDOS of carbon since the lowest unoccupied molecular orbital (LUMO) and the highest occupied molecular orbital (HOMO) states are mainly contributed from the C atoms. The other constituents of $Alq_3$ are Al at the center, N, O, and H which are shown in different colors in Fig. 5.1. The total number of each element in $Alq_3$ molecule with *Gaussian03* assigned numbers as the position of all individual atoms for DOS calculation is given in Table 5.1.

Table 5.1: Total amount of atoms and the assigned numbers in $Alq_3$ molecule:

| Atoms | Assigned numbers | Total number of atoms |
|---|---|---|
| Al | 1 | 1 |
| O | 2-4 | 3 |
| N | 5-7 | 3 |

| | | |
|---|---|---|
| C | 8-34 | 27 |
| H | 35-52 | 18 |

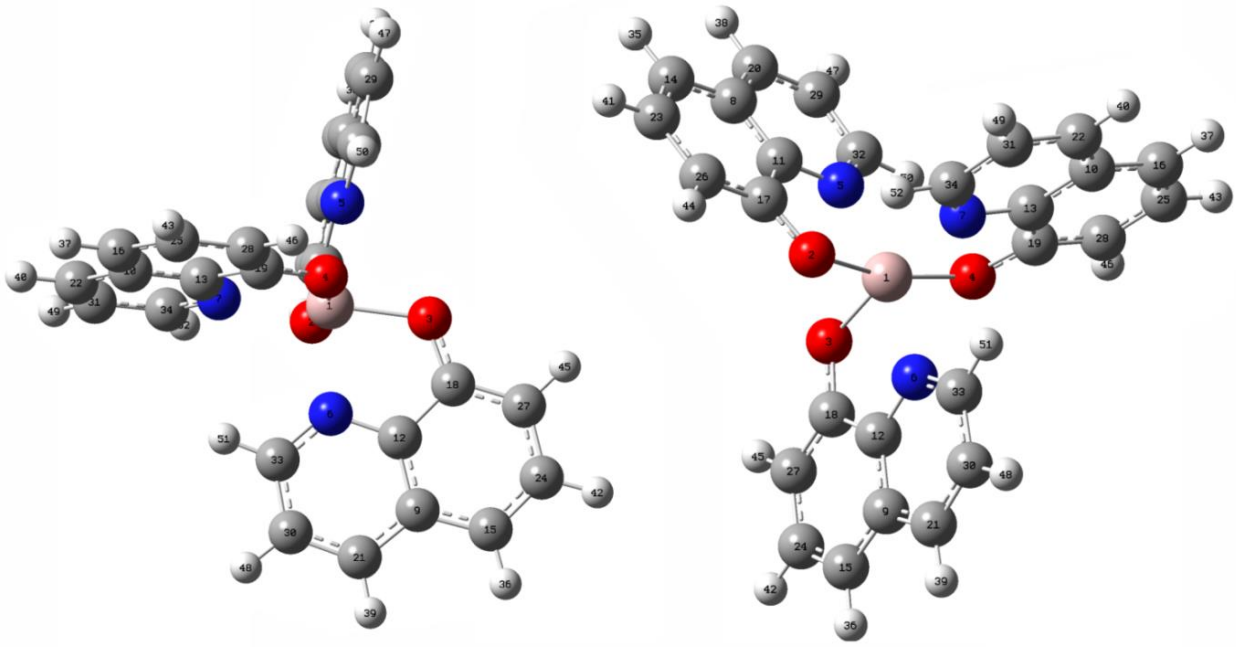

Figure 5.1: Molecular structures of $Alq_3$ in two different angles are shown in order to have a better idea about the shape of non-planar $Alq_3$ molecule. Pink, red, blue, dark gray and light gray circles are corresponded to Al, O, N, C and H atoms respectively.

As shown in Fig. 5.1, the configurations of three 8-hydroxyquinoline ligands are basically identical according to the number of atoms and the bonding between the atoms in each ligand, i.e. same numbers and bonding of atoms, until we consider the angular arrangement between them. With this optimized $Alq_3$ molecular structure, the total density of state (DOS) was calculated and the HOMO and LUMO state were determined. The spatial distribution of LUMO

states is plotted and the LUMO iso-surface is presented in Fig. 5.2. One can see that the LUMO states are clearly localized and seem to be concentrated near the C-C bonds (single or double). An interesting observation is that despite similarity of the three 8-hydroxyquinoline ligands, the LUMO states are not evenly distributed across $Alq_3$ structure. A possible reason of this behavior is because of the asymmetric shape of $Alq_3$ if we look at the angular arrangement between the 8-hydroxyquinoline ligands and the center Al atom with these ligands. There are five different bonding groups involving C atoms in $Alq_3$ and a list of these bonding groups is given in Table 5.2. From the bonding configurations of C-C and C-other atoms listed in Table 5.2, it is clear that all C atoms are $sp^2$ hybridized and contain both σ and π characters. For the direct parallel interaction of the orbitals, the σ-bonds are stronger than the π-bonds, which results in higher energy requirement of breaking a single bond than that of a double bond, which contains an σ-bond and a π-bond. The LUMO is the π* antibonding orbital of the molecule.

Although the LUMO iso-surface in Fig. 5.2 provides intuitive understanding of the localized feature of the LUMO states in $Alq_3$, it is still difficult to determine specifically which carbon atoms or other atoms in that ligand are largely contributing to the LUMO state. However, in Table 5.2, we see that the C atoms in the bonding groups '*A*', '*B*', '*C*' and '*D*', have only single σ-bonds with other atoms and all the center C atoms have C-C double bonds, which are weaker. Therefore from these four groups, one can expect the LUMO will be originated from C-C double bonds; and for group '*E*', it will be C-N double bonds. Also Fig. 5.4, where all the PDOS spectra are shown, if we look at the LUMO position, one can see N also have a higher intensity than other atoms excluding C, which indicates its fair contribution to the LUMO of $Alq_3$. A more detailed analysis of the PDOS for all individual C atoms will be discussed later.

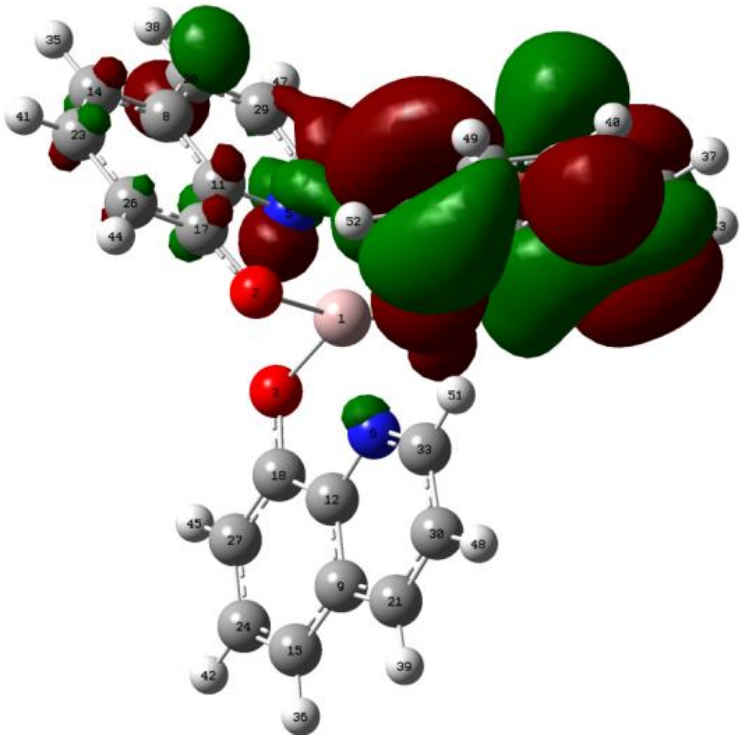

Figure 5.2: Calculated LUMO iso-surface of $Alq_3$ molecule. It is shown that only one 8-hydroxyquinolinato ligand in $Alq_3$ is contributing to the LUMO state. This orbital structure depends on the bonding of C atoms with the other atoms in $Alq_3$.

Table 5.2: Five different bonding groups of C atoms, depending on other atoms connected to it, in $Alq_3$ molecule. The center C atom is bonded with (A) two other C atoms and H atom; (B) two other C atoms and a O atom; (C) three other C atoms; (D) two other C atoms and N atom; (E) C, N and H atoms.

| Serial | Structure | Shortly for easiness |
|---|---|---|
| A | 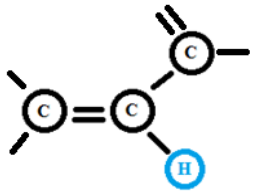 | CCCH |
| B | 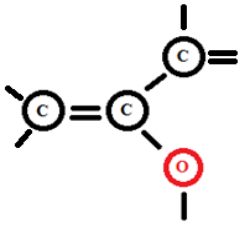 | CCCO |
| C | 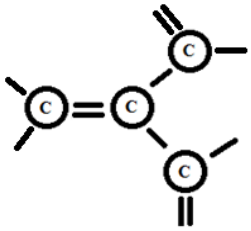 | CCCC |
| D | 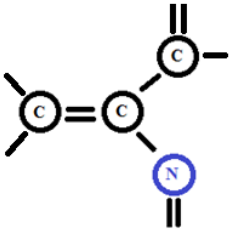 | CCCN |
| E | 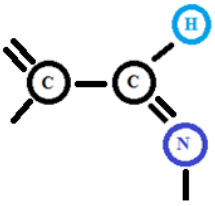 | CCNH |

**5.2: Normalization:**

Before going through the interpretation of the experimental spectra, all the NEXAFS spectra were always normalized. In the experiment, the measured values are influenced by the variation of the incident beam flux which is probed to the samples. It is therefore necessary to correct the measured intensity and performing this is referred to as normalization of a spectrum. Depending on the type of samples as well as detection conditions and beam energy, normalization must be done in different ways; such as, dividing the measured spectra by the signal recorded simultaneously from a reference grid while experimenting the samples or, by the signal recorded from a separate sample [36]. In present study, the absorption spectra are divided by the incident intensity measured using a photodiode- a device placed in the sample chamber which can measure the same beam intensities the samples receive in the chamber. This alternative system is set up because the incoming photon flux $I_0$ measured at the SGM beamline of CLS is not ideal to use for normalizing the C spectra. When experiments for this study were carried out, a gold mesh was used to measure the $I_o$ but it was considered to be contaminated by hydrocarbon. This means that, when the incoming photons hit the gold mesh, hydrocarbon molecules on the gold mesh would absorb the incoming photons and result in unwanted relative absorption intensity which contains unexpected fluctuations in the $I_0$ measurements. Therefore, normalizing the TEY and TFY values by the beam current $I_0$ can make a large amount of errors by removing several important features from the spectra. Hence, rather than using $I_0$ measured by the gold mesh, normalization using photodiode is highly preferable and was done in this research.

### 5.3 Interpretation of Experimental and Calculated Spectra:

Now the NEXAFS and calculated DOS spectra of C atoms are discussed in the following.

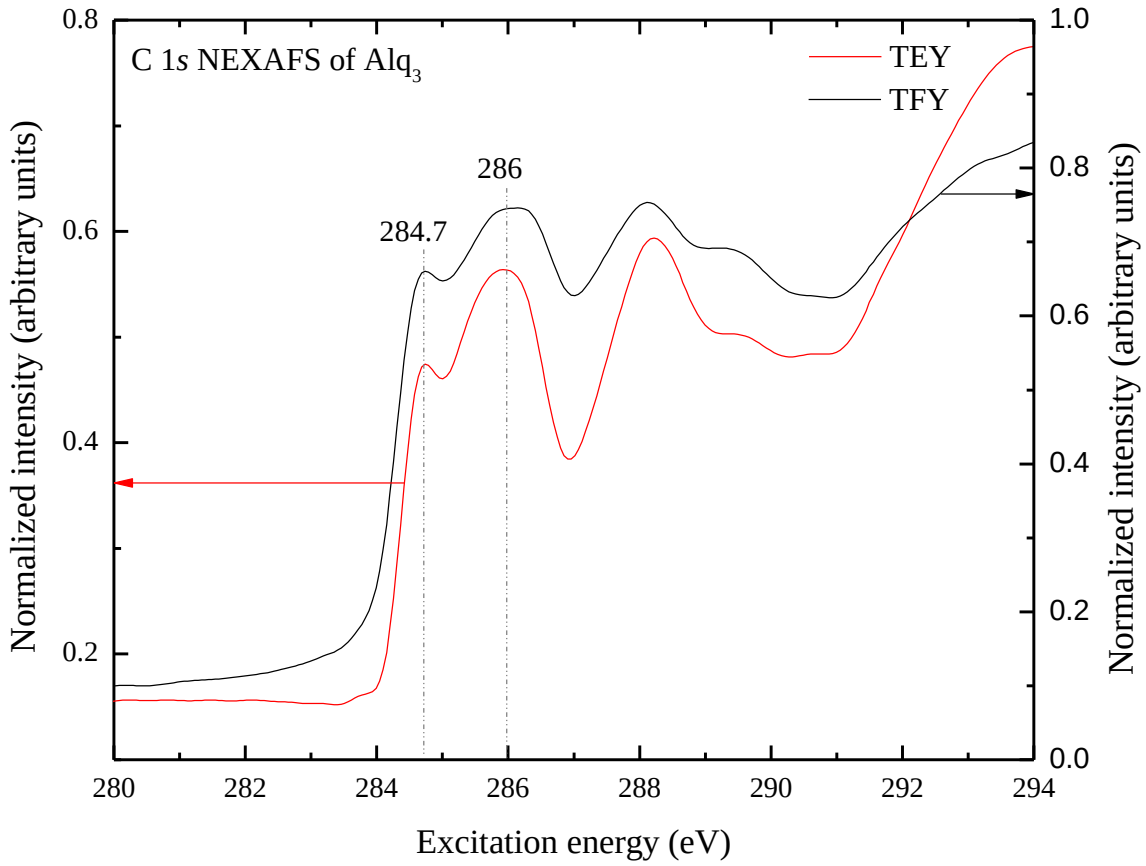


Figure 5.3: Carbon 1*s* NEXAFS spectra (TEY and TFY) of pristine $Alq_3$ reference material. The LUMO state is located at 284.7 eV for both of the TFY and TEY. The left and right Y-axes correspond to the TFY and TEY spectra respectively.

In the Fig. 5.3 the Y-axis values are shown which can be used to compare the peak heights, however, it should also be noted that Y-axis data does not reflects the actual measured raw counts as these spectra are normalized. For the other figures after Fig. 5.3, the Y-axis values are not shown as discussion about the relative intensities are not provided in this thesis.

Fig. 5.3 shows C 1*s* NEXAFS spectra for pristine $Alq_3$ reference sample taken in the surface-sensitive total electron yield (TEY) and bulk-sensitive total fluorescence yield (TFY) modes. The first peak at 284.7 eV is assigned to the LUMO state and LUMO+1 state is located around 286 eV. From the fact that the energy and intensities of the TEY and TFY spectra are very much identical, it can be said that the bulk $Alq_3$ is pure. However, the LUMO+1 peak of the C 1*s* TFY spectrum is slightly wider than that of the TEY spectrum or conversely, we can also say LUMO+1 TEY spectra is slightly sharper in intensity than TFY. A more detailed discussion on the experimental spectra has been done in the following.

Fig. 5.4 shows the PDOS spectra of the constituent elements of $Alq_3$. The calculated spectra were broadened by convolution with Gaussian functions with a full width half maximum (FWHM) of 0.2 eV. One can see that the LUMO state of the C atoms shows relatively large intensity, as expected, and nitrogen also shows a significantly large intensity compared to other atoms except C in $Alq_3$.

Fig. 5.5 shows a comparison between experimental C 1*s* TEY spectrum of pristine $Alq_3$ film and calculated PDOS spectrum of C in $Alq_3$. The *x*-axis energy of the PDOS spectrum was shifted to the experimental energy positions and the first peak of the PDOS spectrum was set to the experimental energy position of the LUMO state. The PDOS spectrum was broadened by Gaussian convolution with FWHM of 0.3 eV. It can be seen that the calculated intensity and energy position for LUMO and LUMO+1 peaks have fairly good consistency with experimental results. This comparison has been done in order to validate the calculated spectra and also to explain the LUMO and LUMO+1 states more specifically relating to the individual C atoms in $Alq_3$.

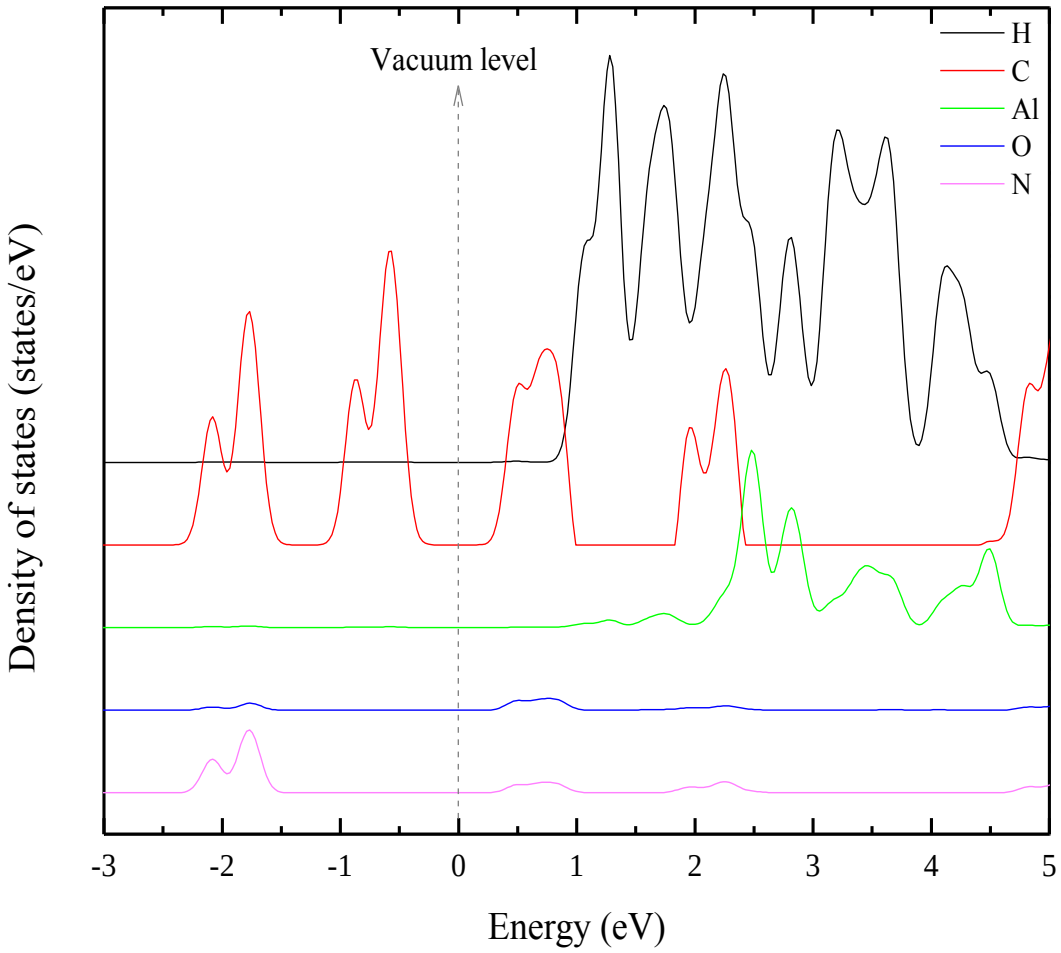


Figure 5.4: Calculated density of states (DOS) of all constituent elements of $Alq_3$.

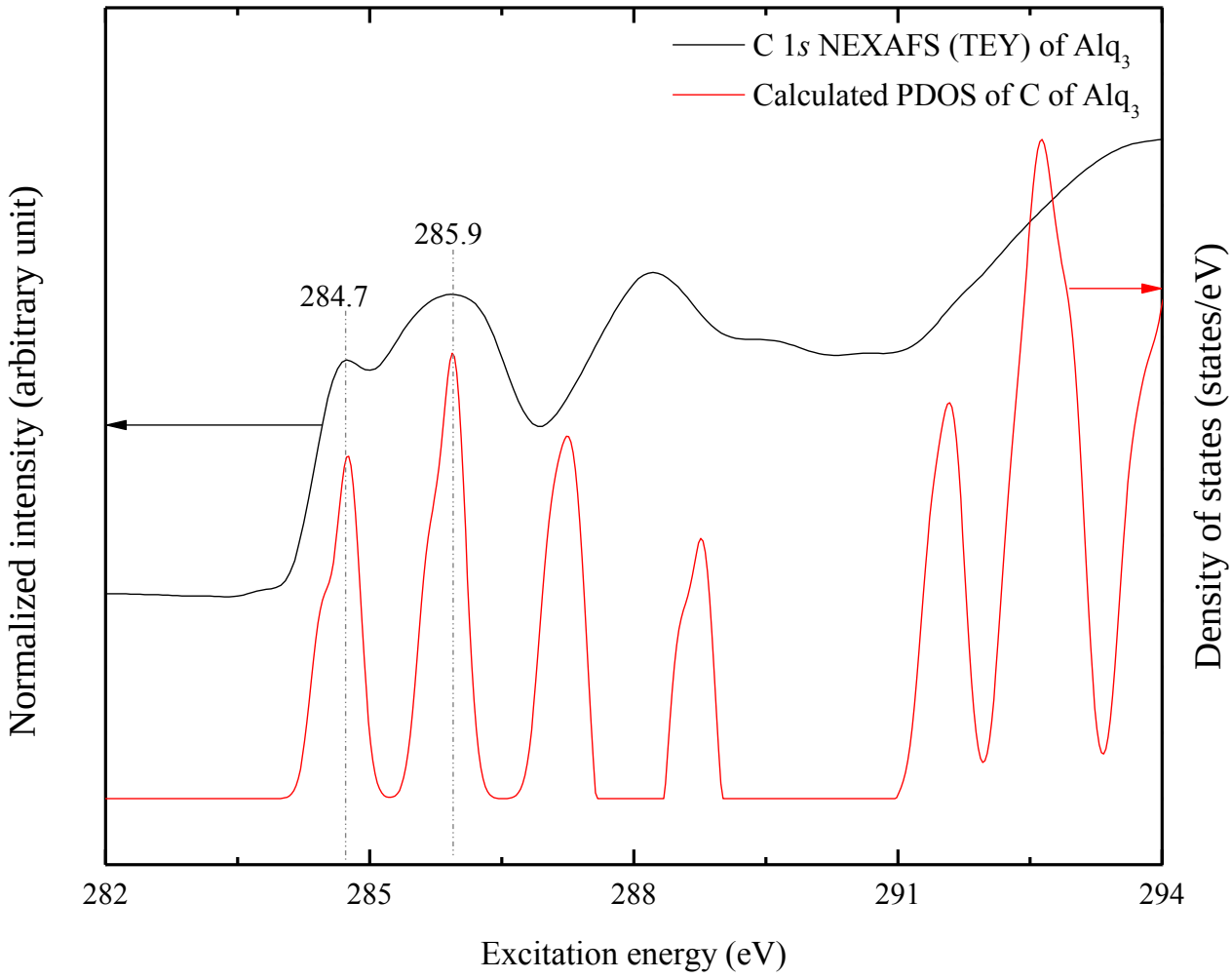


Figure 5.5: Calculated partial density of C states and C 1*s* NEXAFS (TEY) spectrum of $Alq_3$. The energy positions of the spectral lines are fairly consistent with the calculated DOS. The left and right Y-axes correspond to the TEY and PDOS spectra respectively.

Before approaching more specific discussion of the LUMO and LUMO+1 of the experimental C 1*s* spectra, we will check the experimental spectra of the Co deposited sample. First consider the C1*s* TEY spectrum of the $Co/Alq_3/SiO_2$ with that of the bulk $Alq_3$ sample (see appendix Fig. A-1), it does not look legitimate to compare because of the low intensity dip at the start of the TEY spectrum of $Co/Alq_3/SiO_2$. The LUMO and LUMO+1 position are not clear and have reduced intensities and possibly the intensities as a whole of this spectrum are suppressed highly by that dip. It is assumed that the dip in the TEY spectrum here could be a result of carbon contamination at the gold mesh of the apparatus of the beamline at the time of NEXAFS measurement on $Co/Alq_3/SiO_2$ at the CLS as we discussed earlier. Considering this, one may like to see a second derivative of the TEY spectral line for $Co/Alq_3/SiO_2$, which is done and shown in the appendix Fig. A-2. Surprisingly, in Fig. A-2, the derivative spectral line shows that there is a peak at 284.7eV which is found as the LUMO in TFY spectra of $Co(top)/Alq_3$ (Fig. 5.6), same as the LUMO for $Alq_3$ before Co deposited onto it. The lower intensity of the LUMO and LUMO+1 could also be a result of Co diffusion into the $Alq_3$ and the intensity of the dip caused by the contamination is large enough to hide this peak position. The unchanged position of the LUMO found from the second derivative of the C 1*s* TEY spectrum after Co deposition onto $Alq_3$, of the LUMO peak suggests that there is no major carrier transfer occurred between $Alq_3$ and Co in this region. However, for LUMO+1 or further detailed discussion we cannot rely on this spectrum and therefore for our future analysis, the TFY spectra, which is unaffected by the C contamination at the beamline mesh, has been used.

Looking to Fig. 5.6, we see that the LUMO peak in the $Alq_3$ is constant in energy position after depositing Co onto it, the LUMO+1 of the $Alq_3$ is broad, unlike $Co/Alq_3$. Whether

the broad peak contains several peaks or a single peak or not, we can easily determine through a second derivative of the spectrum.

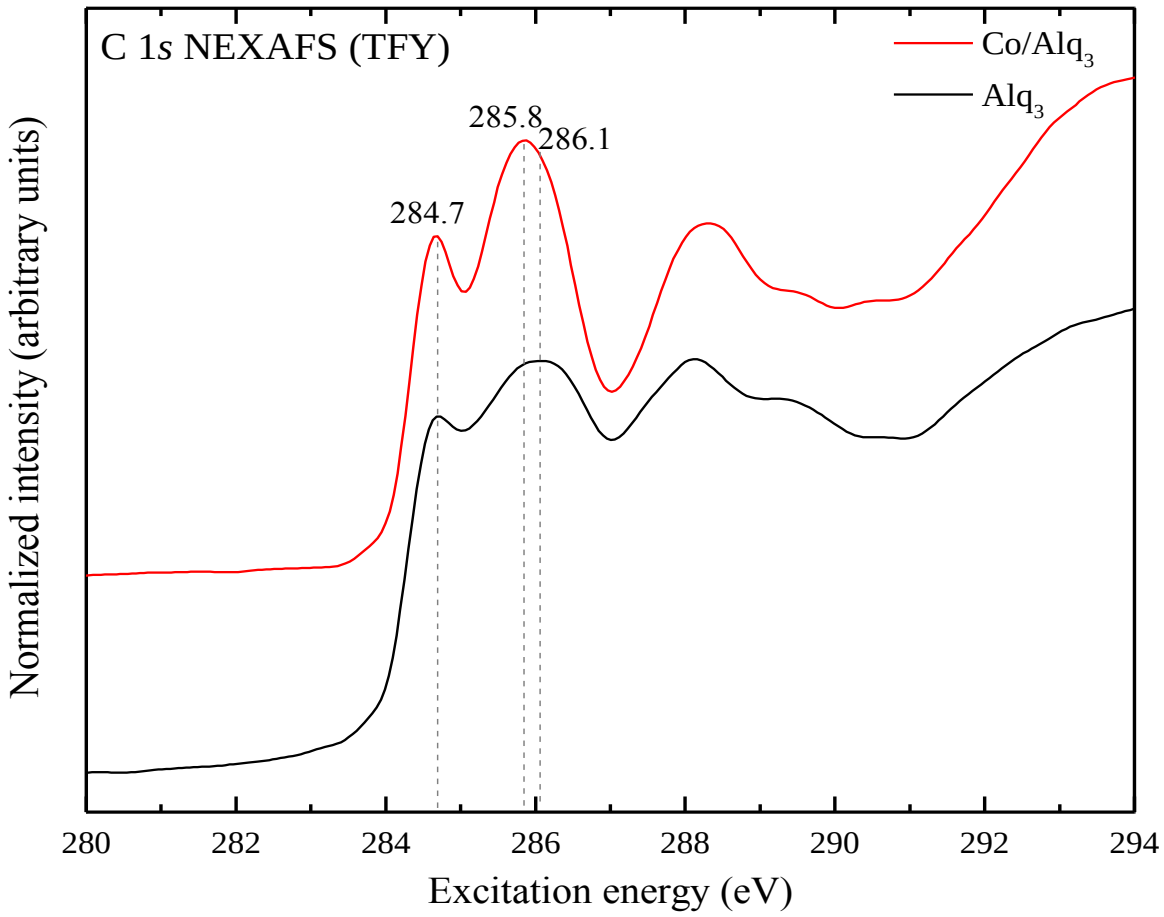


Figure 5.6: C 1*s* NEXAFS spectra (TFY) of pristine $Alq_3$ layer and $Co/Alq_3$ bilayer. The LUMO is found at 284.7 for both samples while the LUMO+1 peak of $Co/Alq_3$ is located at slightly low energy of 285.8 eV with respect to that of pristine $Alq_3$ sample (286.1 eV).

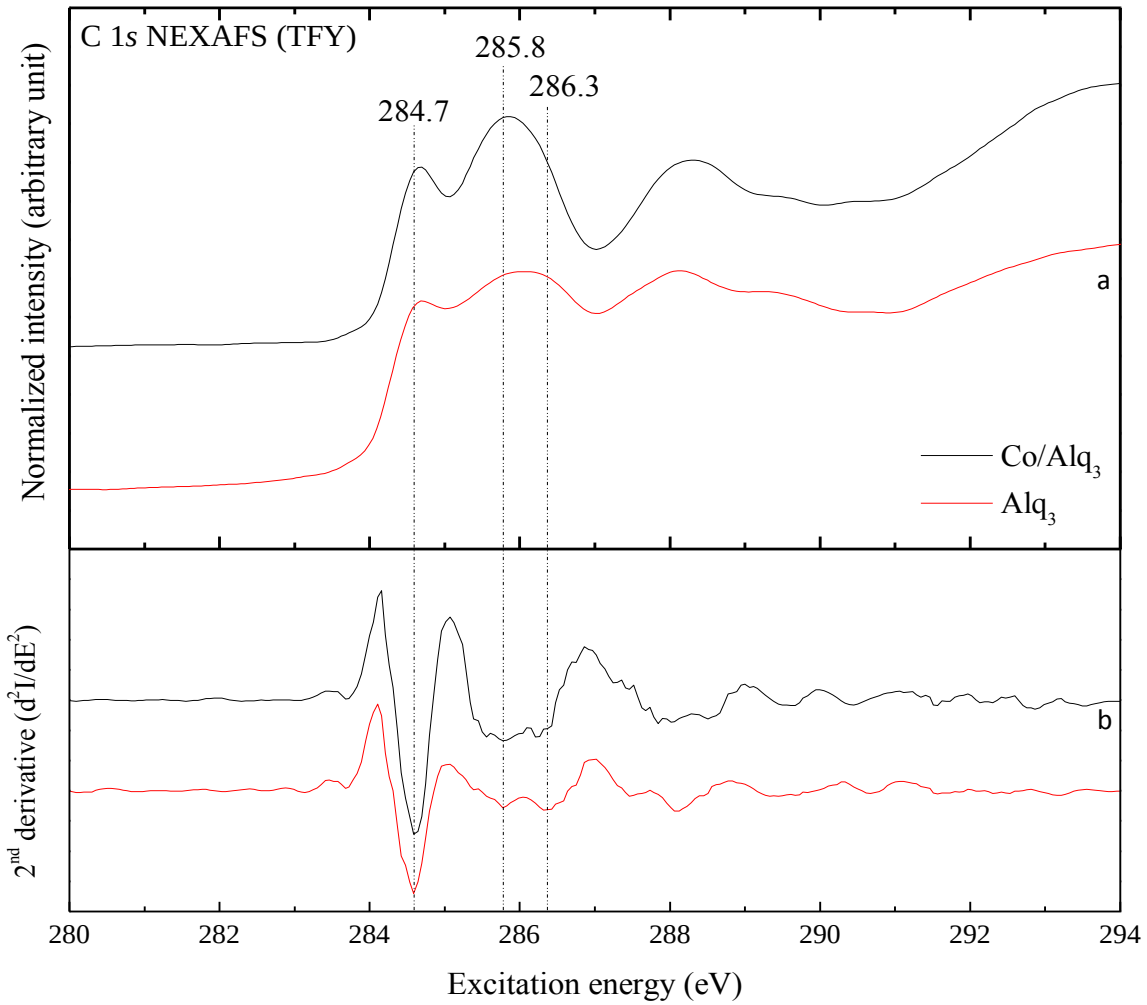


Figure 5.7: (a) C 1*s* NEXAFS spectra (TFY) of Co(top)/$Alq_3$ and pristine $Alq_3$ and (b) second derivative of the corresponding NEXAFS spectra.

Fig. 5.7 shows the second derivatives of the C 1s TFY spectra. In this figure, it has been found that the first peak of the C 1*s* spectra of the pure $Alq_3$ sample is located at 284.7 eV and the second peak is actually a combination of two peaks at 285.8 eV and 286.4 eV respectively. Therefore, this second peak is LUMO+1 and LUMO+2 combined together. Now comparing these peaks in the same figure with the TFY spectra of C 1*s* of Co/$Alq_3$ sample we can see that the LUMO is at the same position as in the TFY spectra of pristine $Alq_3$. However, in the third

peak, considering LUMO+2 found from the second derivative in Fig. 5.7, the LUMO+2 is suppressed or gone entirely in the spectra of Co/$Alq_3$ after Co deposition. This is probably the effect of the Co deposition onto $Alq_3$ that may result the electron transfer occurred from Co to $Alq_3$ material and thus makes the LUMO+2 states unavailable in the Co/$Alq_3$ bilayer struture. From the above discussion we may conclude that the Co atoms have a preferential site when deposited onto $Alq_3$ and it affects the localized LUMO+2 states, leaving unaffected LUMO and LUMO+1.

The next approach is used to determine the preferable sites by analyzing the position of the C atoms. From the theoretical PDOS calculation of C atoms showed in Fig. 5.8 one can determine which C atoms from which bonding groups (Table 5.2) contribute to the LUMO, LUMO+1 and LUMO+2 levels. By doing this, we will be able to detect the possible unaffected and affected sites of the $Alq_3$ by the Co deposition. From the Fig. 5.8 where all the C atoms' PDOS are shown, we can categorize these 27 C atoms according to the contribution and intensities of these C atoms' found in the LUMO and LUMO+1 level of $Alq_3$. The intensities of the Fig. 5.8 are normalized individually for the better view of all the spectra. First we have seen in Fig. 5.8 that there is no C atom in $Alq_3$ which is only contributing to the LUMO+1 or LUMO+2 without having a contribution to LUMO, i.e. all C atoms are contributing to the LUMO, however, not all can be found in the LUMO+1 or LUMO+2. Previously in Fig. 5.5 we have seen after aligning the two spectra (C1*s* TFY and calculated total PDOS of $Alq_3$), that the LUMO and LUMO+1 peaks in the calculated PDOS contain shoulder, which suggest that first peak (LUMO) and second peak (LUMO+1 and LUMO+2) of calculated PDOS are combination of multiple closely related C atoms of equal or close energies. The second derivative of the spectra in Fig. 5.7 however shows a single peak for the LUMO. Therefore, when compared the

calculated and experimental spectra, the first peak all the individual carbon atoms' PDOS are considered as LUMO and second peak is in however is LUMO+1 or LUMO+2, depending on the C atoms, which will be found after comparing the energy position of the PDOS according to the experimental spectra.

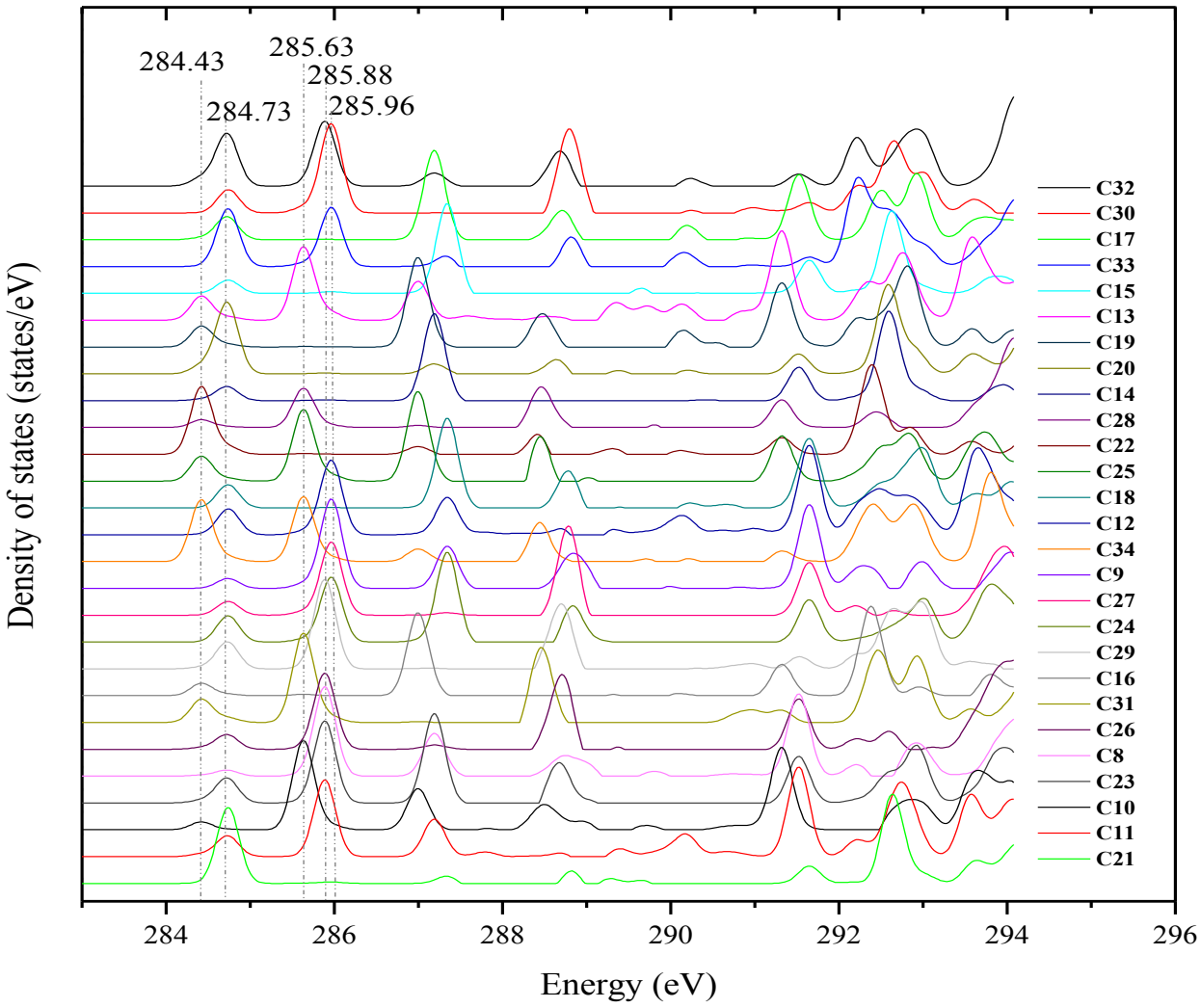


Figure 5.8: The partial density of states (PDOS) of all individual C atoms of $Alq_3$. The x-axis is set with the experimental energy in order to assign the responsible carbon atoms in LUMO of $Alq_3$.

Recall that after Co deposition only the LUMO+2 of C atoms seem affected. One can assume that the charge transfer from Co to $Alq_3$ could affect the LUMO and LUMO+1 also if LUMO+2 affected. It is not necessarily true because we have seen from the iso-surface picture in Fig. 5.2 that the unoccupied states in this molecule are localized. Therefore, the effect may not be necessarily to the entire unoccupied states but only to a specific localized unoccupied state. This charge transfer is very low compared to the available free electron in the metallic Co, and hence is not affecting the Co $L_{2,3}$ spectra showed in Fig. 5.14.

Now, from Fig. 5.8, the positions of the C atoms which have LUMO+1 states available are 13, 28, 25, 34, 31 and 10. For LUMO+2, C atoms of positions 32, 30, 33, 12, 9, 27, 24, 29, 26, 8, 23 and 11 are responsible. From this one can see that there are more C atoms contribute to LUMO+2 (two times) than LUMO+1. These two C atoms which can be found to contribute to LUMO+2 is our concern and we can say that after deposition of Co on $Alq_3$ these 12 C sites out of total 27 C atoms are affected only.

Now, consider the bonding structure of these C atoms, with the other atoms in $Alq_3$ so that we can define which C atoms from which bonds are basically responsible for LUMO+2 states. In Fig. 5.9 to 5.13 below, the PDOS of five different local carbon environments are shown.

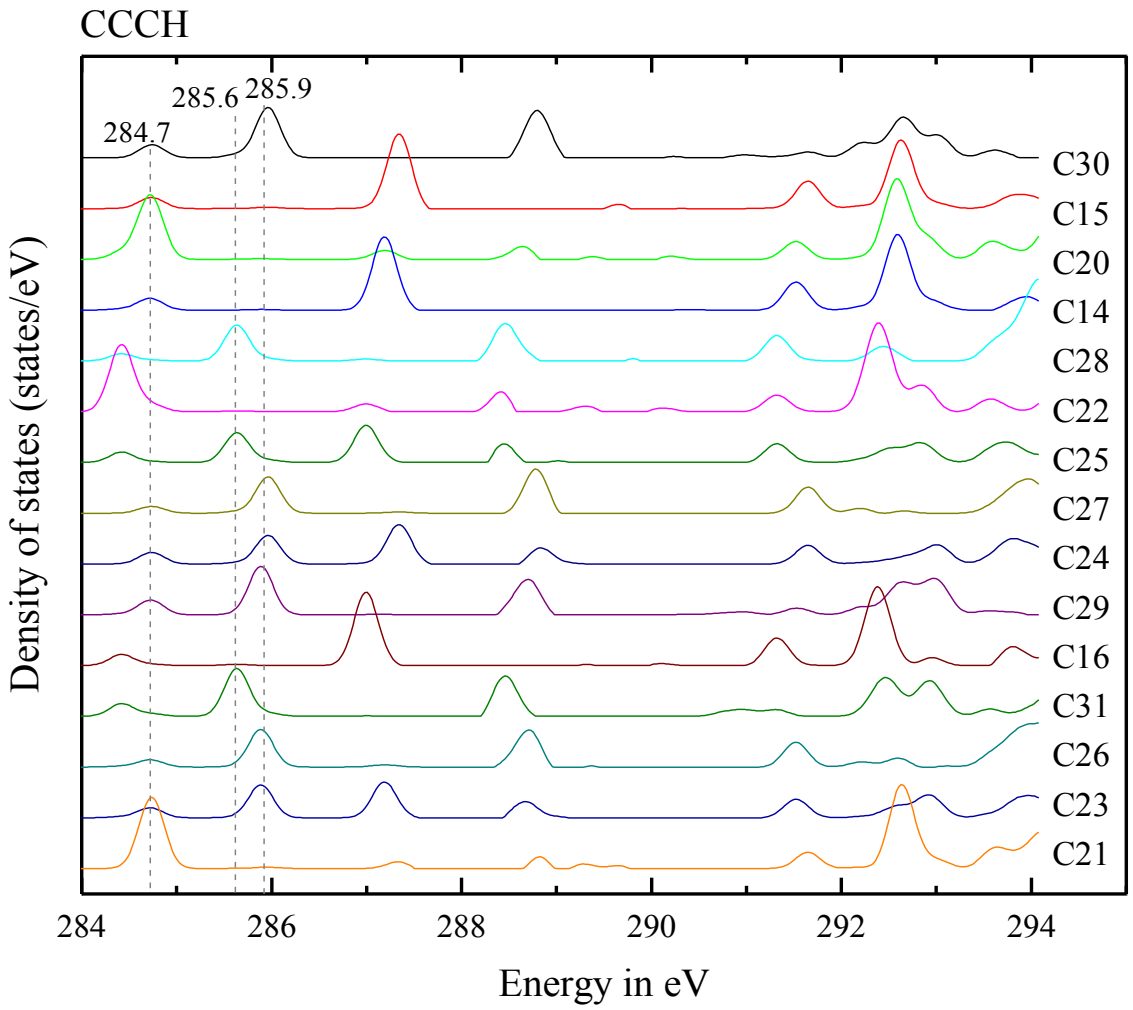


Figure 5.9: The partial density of states (PDOS) of carbon atoms in $Alq_3$, those have the same types of bonding structure, CCCH. The *x*-axis is set with the experimental energy in order to assign the responsible carbon atoms in LUMO of $Alq_3$.

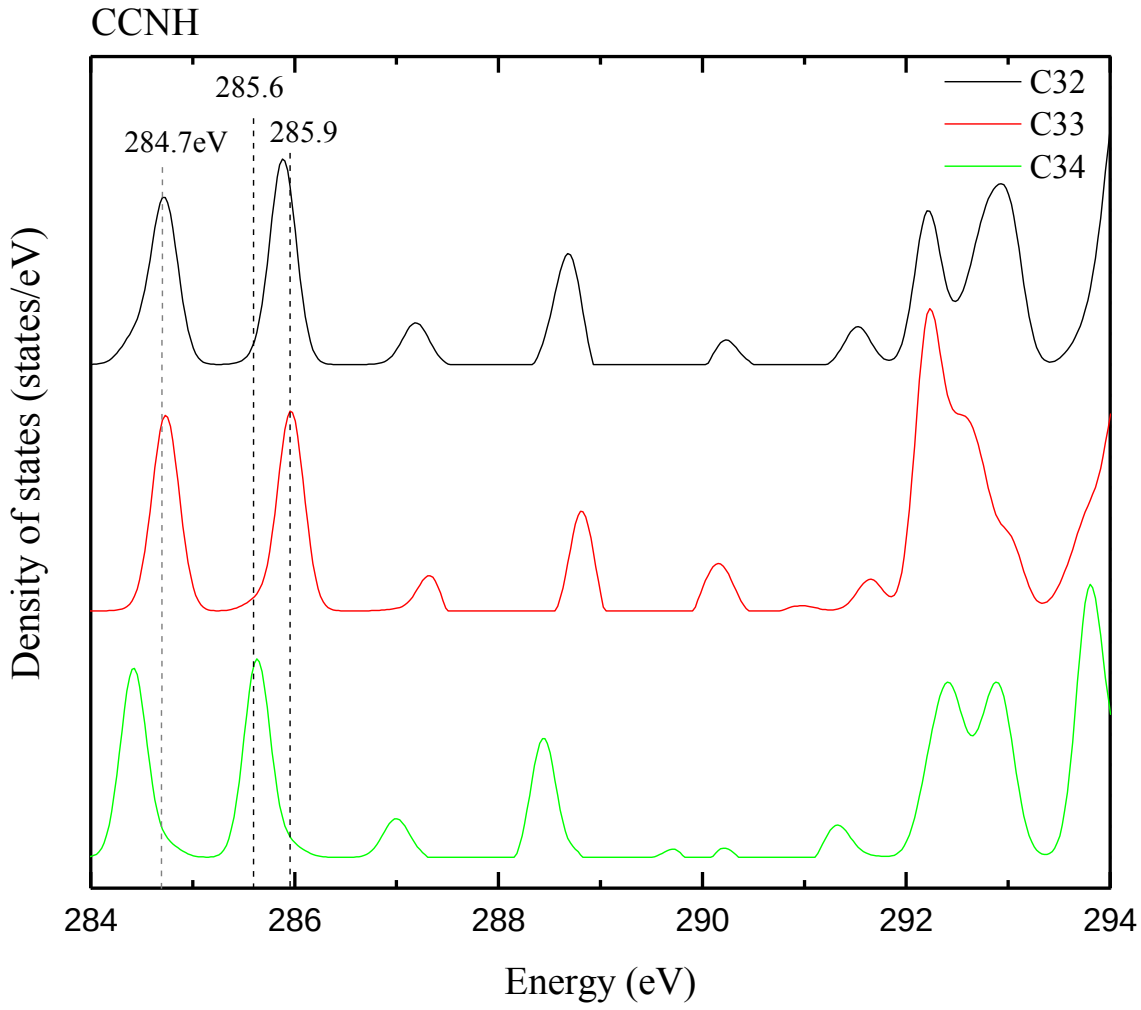


Figure 5.10: The partial density of states (PDOS) of carbon atoms in $Alq_3$, those have the same types of bonding structure, CCNH. The *x*-axis is set with the experimental energy in order to assign the responsible carbon atoms in LUMO of $Alq_3$

.

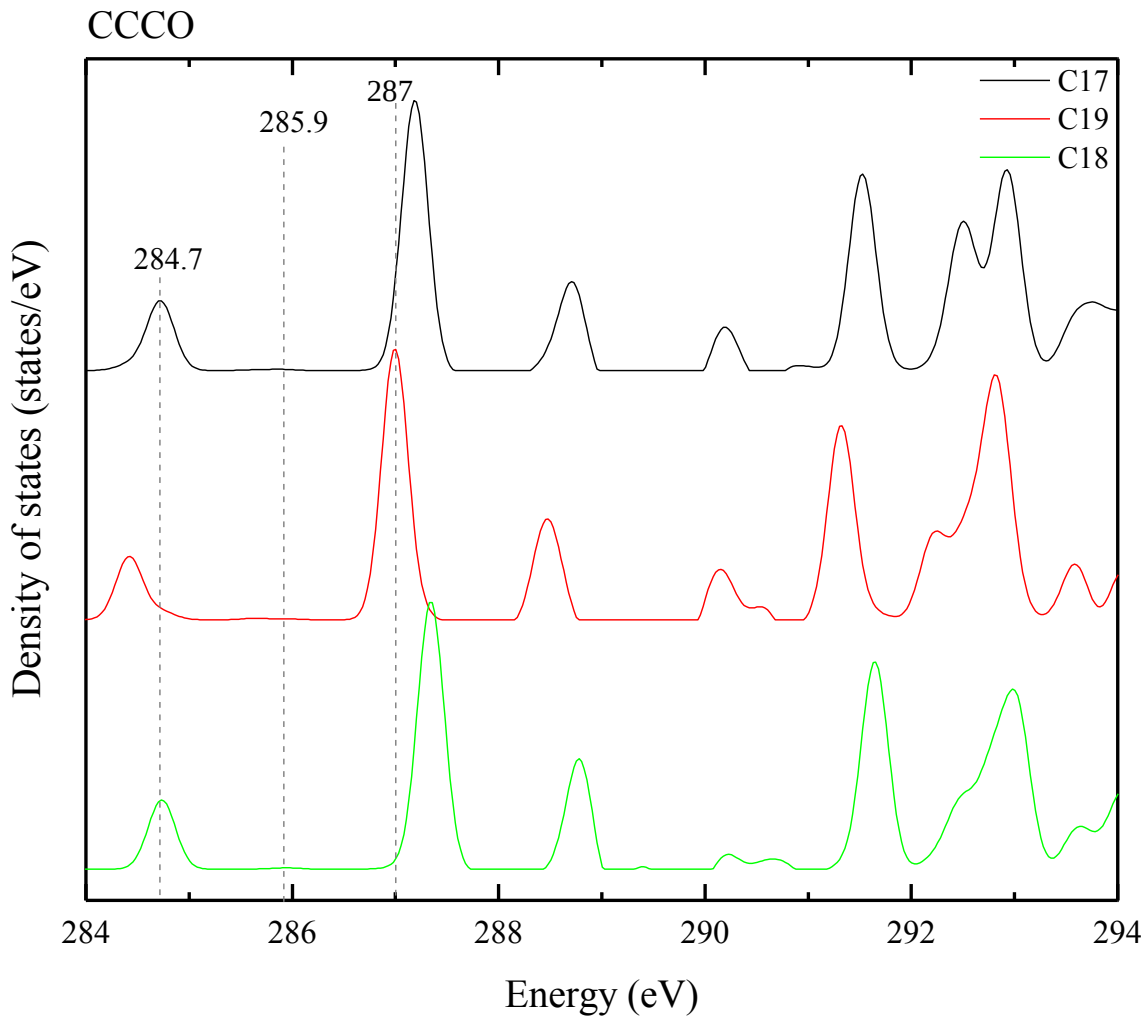


Figure 5.11: The partial density of states (PDOS) of carbon atoms in $Alq_3$, those have the same types of bonding structure, CCCO. The *x*-axis is set with the experimental energy in order to assign the responsible carbon atoms in LUMO of $Alq_3$.

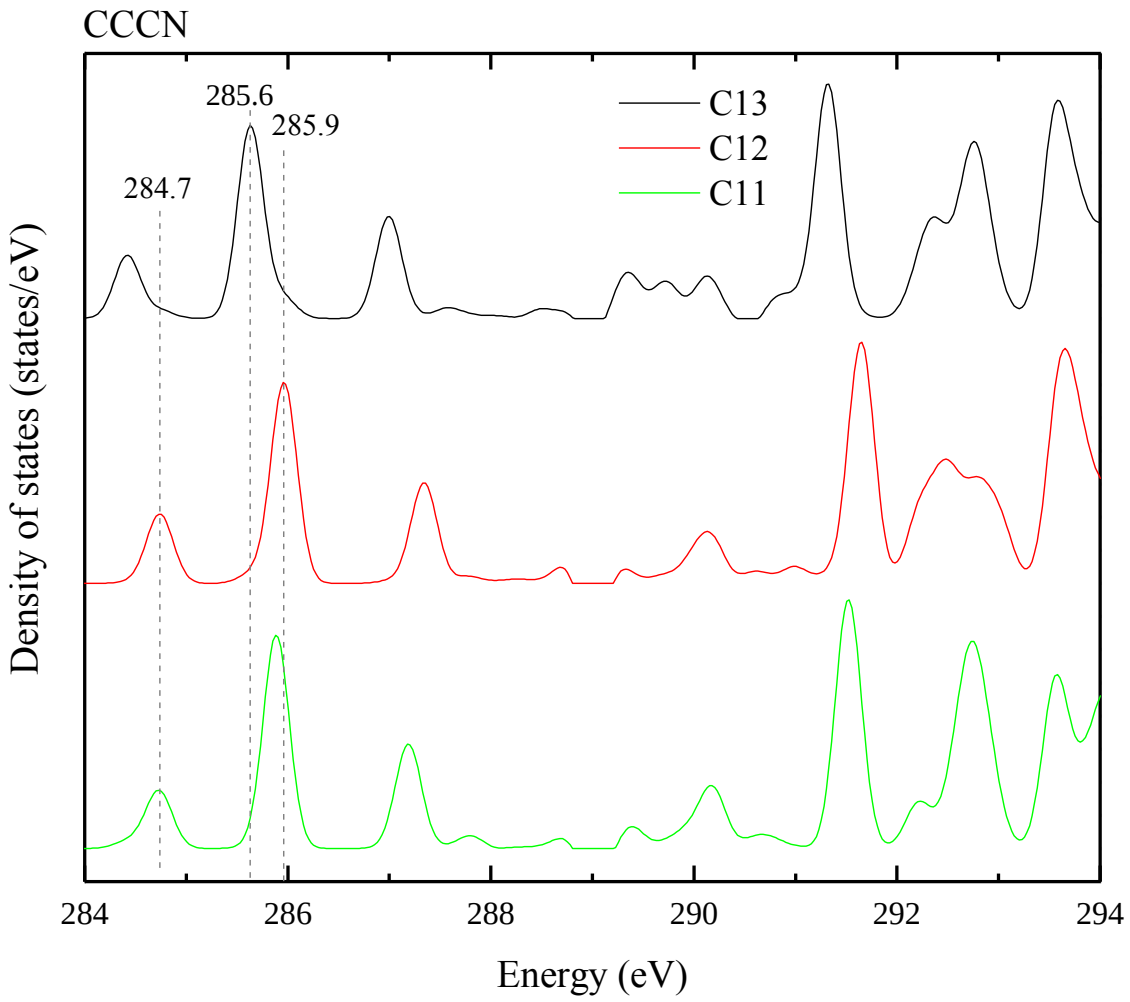


Figure 5.12: The partial density of states (PDOS) of carbon atoms in $Alq_3$, those have the same types of bonding structure, CCCN. The *x*-axis is set with the experimental energy in order to assign the responsible carbon atoms in LUMO of $Alq_3$.

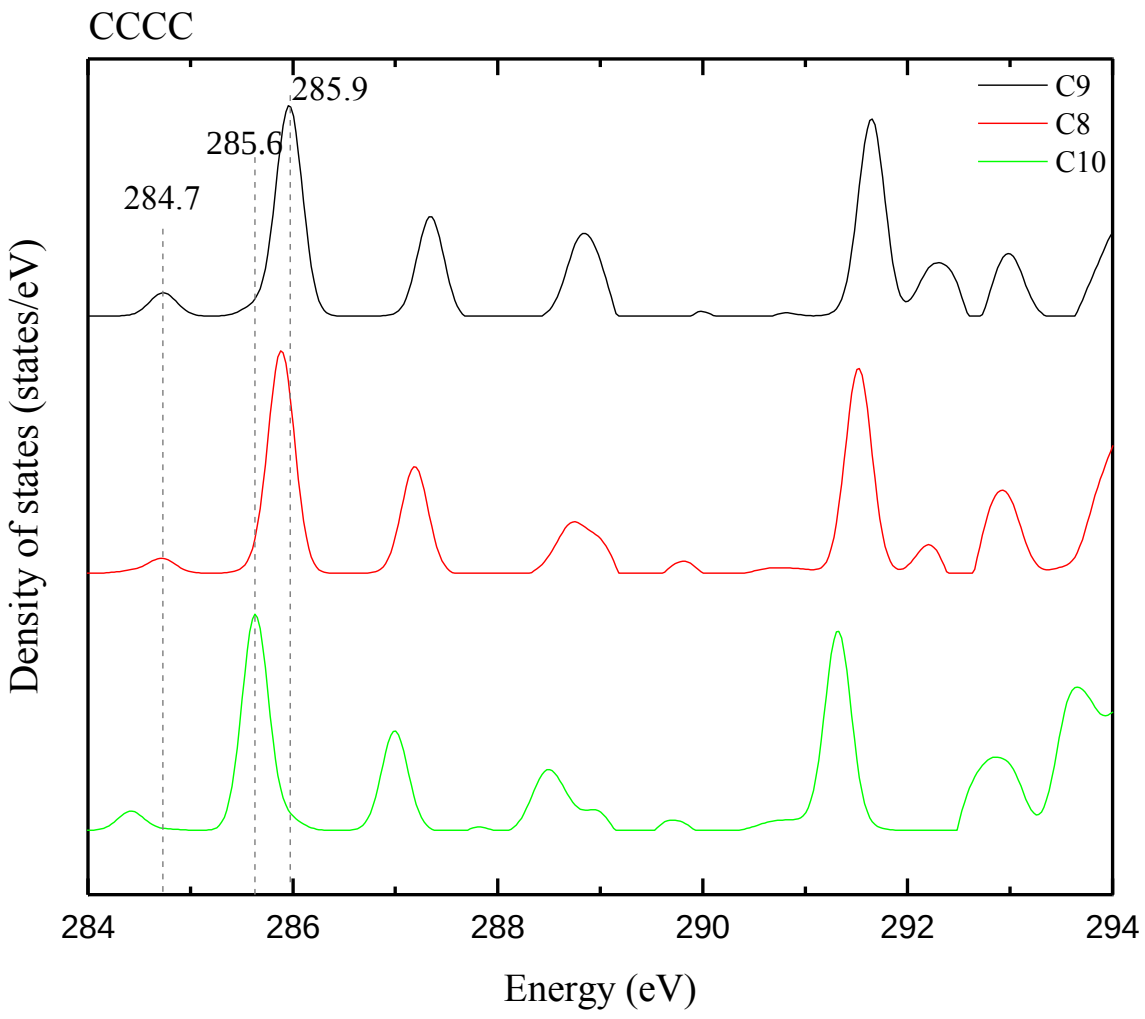


Figure 5.13: The partial density of states (PDOS) of carbon atoms in $Alq_3$, those have the same types of bonding structure, CCCC. The *x*-axis is set with the experimental energy in order to assign the responsible carbon atoms in LUMO of $Alq_3$.

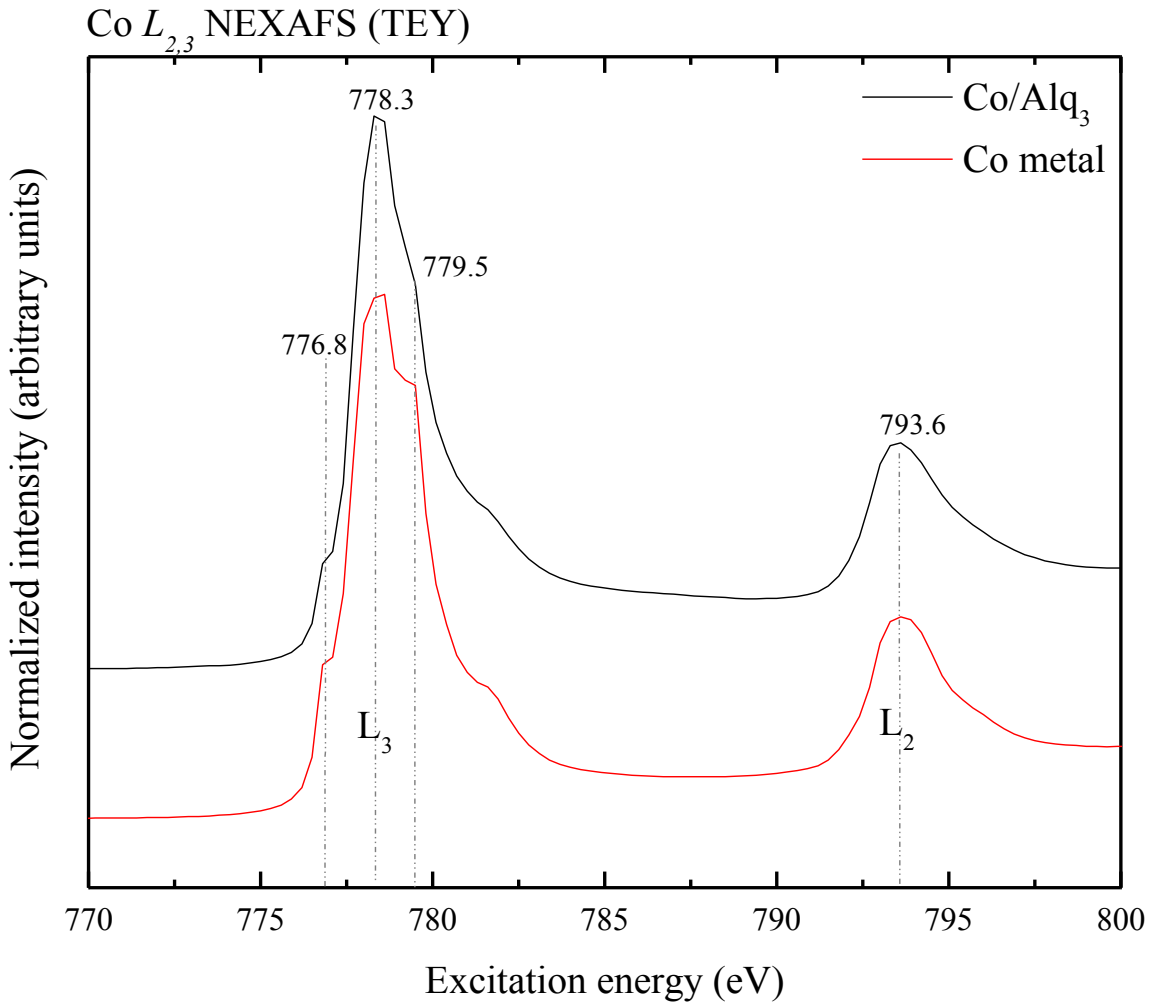


Figure 5.14: Co 2*p* NEXAFS spectra (TEY) Co 2*p* of Co metal and Co/$Alq_3$/$SiO_2$. The shoulder picks at 776.8 and 779.5 eV are the result of oxidation of Co.

From Fig. 5.9, one can see the position 30, 27, 24, 29, 26 and 23 of C atoms are the center atoms (see Table 5.2 for the structure) of CCCH bonding; From Fig. 5.10, where PDOS for CCNH are shown, the position 32 and 33 of C atoms are the center two out of three CCNH bonding in $Alq_3$; From Fig. 5.12, 12 and 11 positions of C atoms comes from CCCN bonding and finally, C atoms of position 9 and 8 are comes from CCCC bonding groups (Fig. 5.13). We also see that no significant contribution to LUMO+2 coming from any of the center C atoms

from CCCO bonding group (Fig. 5.11). Hence, we can say that these C atoms, bonded to O atoms, in $Alq_3$ are also unaffected after the Co deposition, though Co is sensitive to oxygen and may form CoO or $Co_2O_3$. But forming of these Co oxides inside the $Alq_3$ possibly requires molecular breakage to form Co and O bonds which is not the case happened in the experiments in this research. Also the Co $L_{2,3}$ spectra in Fig. 5.14 suggests that the Co is metallic after the deposition.

From the molecular structure of $Alq_3$, it is clear that the three ligands of the $Alq_3$ contain an equal amount of carbon and other atoms. The types of bonding structure of C-C and C-other atoms generally looks very similar. However, the angular arrangement with the center atom may need to be considered which made the three ligands unequal depending on the interaction with other molecules or atoms, e.g. Co here. Five types of bonding are present in each ligand and we have seen that Co affects three bonding structures equally, and leaves one unaffected. We have found that the most of the affected C atoms (i.e. six out of twelve C atoms) come from CCCH bonding group. The reason for this could be because most of the bonding in $Alq_3$ is CCCH bonding type, and therefore comparably a larger effect is expected. One may think that these 12 C sites may be distributed equally to all the three ligands (e.g. 2 in each ligand); however, this is not true. From the picture of molecular structure of $Alq_3$ in the Fig. 5.1, It has been found that the 12 C atoms, which are said to contribute to the LUMO+2, are comes from two ligands of $Alq_3$ and the third ligand, which mostly contribute to the LUMO, has no LUMO+2 C sites found from the DFT calculations. Fig. 5.15 is showing the $Alq_3$ molecular structure with the results found from the analysis of the DFT calculated DOS spectra.

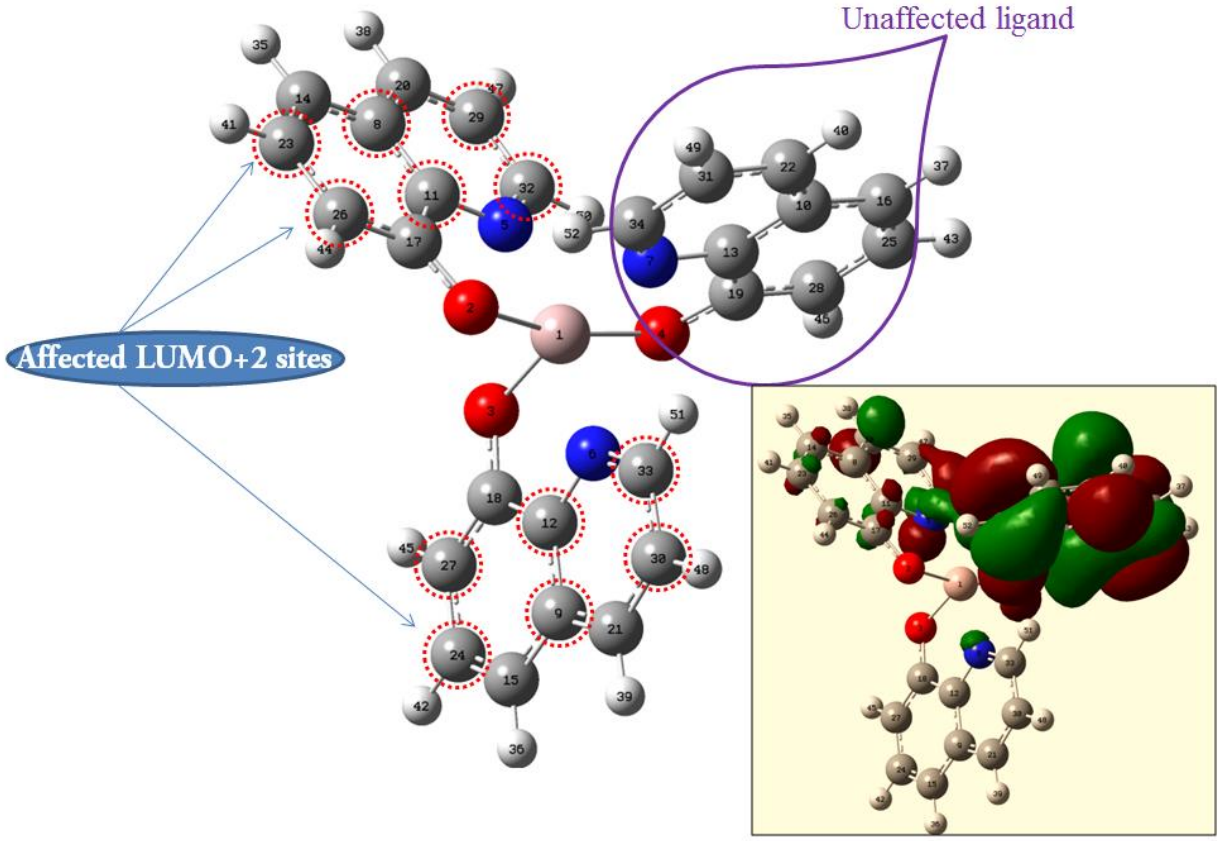


Figure 5.15: $Alq_3$ molecular structure with LUMO and LUMO+2 sites. Inset is showing the LUMO iso-surface coming from the unaffected ligand.

Hence, we can conclude that these ligands, containing LUMO+2 sites of the $Alq_3$, are the most preferable choice for Co interactions to the $Alq_3$ material. An explanation of this choice by Co could possibly be related to the asymmetric structure of $Alq_3$. Generated LUMO iso-surfaces by the *Gaussian03* arise mainly from one ligand out of three show proof that these structurally alike ligands are in fact totally different in nature and must interact unequally with other materials. A question may also arise that whether or not further deposition of Co could affect all the ligands equally or not. The reported $Alq_3$ molecular size is about 1 nm [16] and in this research, the thickness of the Co is ~8nm which is enough to cover the surface of $Alq_3$ properly

and further diffusion into the $Alq_3$ is improbable. Therefore, the effect of the Co on $Alq_3$ discussed here can be expected to be maximized.

# CHAPTER 6

# SUMMARY AND FUTURE WORK

The interfacial electronic structure configuration of organic semiconductor ($Alq_3$) and ferromagnetic metal (Co) bilayered system has been investigated employing synchrotron-radiation X-ray spectroscopy. Co(top)/$Alq_3$ and $Alq_3$(top)/Co bilayered thin films representing a rough interface due to Co diffusion and a sharp interface (expected in $Alq_3$(top)/Co), respectively were prepared by PVD. Spectroscopic results indicated that Co atoms diffused into the $Alq_3$ semiconductor layer during the Co deposition onto $Alq_3$ in agreement with literature findings. According to the results reported by other groups, this diffusion of Co in $Alq_3$ can form a mixed layer with a thickness up to 100 nm and thus results in the modification of $Alq_3$ electronic properties [4]. The measured C 1*s* NEXAFS spectra of Co(top)/$Alq_3$ bilayer film suggested that the LUMO and LUMO+1 of $Alq_3$ are not affected by the Co deposition into $Alq_3$ layer. As the soft X-ray beam is directed from the Co side, we expect that it does not reach to the bottom of $Alq_3$ and as a result both TEY and TFY contain information mainly from the interfacial region of Co and $Alq_3$. Our results clearly indicated the metallic Co cluster penetration into the $Alq_3$ material after Co deposition on top of $Alq_3$ which agreed the results from other researchers [4]. The charge transfer occurred between the two materials for which LUMO+2 of $Alq_3$ is mainly affected.

Another analytical approach has been made to determine the preferred site by the Co in $Alq_3$ molecule. It has been found that 12 C atoms are responsible for the LUMO+2 states of $Alq_3$ and hence these C atoms are assumed to be affected by the Co. Moreover, according to the bonding structure of C with other atoms in the $Alq_3$, it is found that C atoms connected to the O

atoms in $Alq_3$ remain unaffected by the Co deposition and the effect is larger in one ligand out of three ligands in $Alq_3$. The bonding 'C', 'D' and 'E' discussed in chapter 5 (table 5.2) have equal effect from the Co deposition.

For a more detailed analysis of Co on $Alq_3$ the TEY measurements are necessary. In our research the contamination of the gold mesh at the SGM beamline while doing the Co/$Alq_3$ experiment caused the intensity suppression on the TEY spectra of C 1*s* NEXAFS. Using the results of this research, a further study on the Co/$Alq_3$ by X-ray absorption spectroscopy with variable thickness of Co and $Alq_3$ can also be done for a better understanding for organic spintronic device applications. Additionally, the results from this work could help future research on the FM-organic semiconductor interface relating to the spintronic devices performance to focus on more site specific analysis.

# APPENDIX

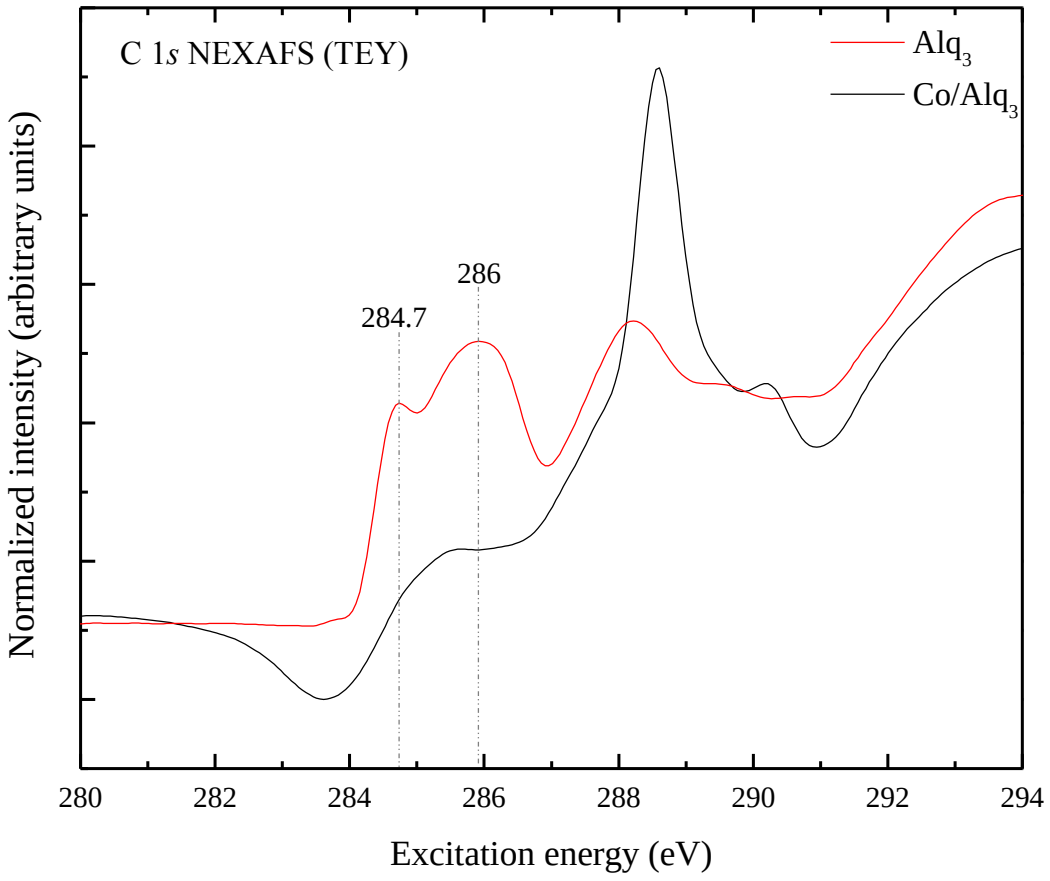


Figure A-1: C 1*s* TEY spectra of $Co/Alq_3$ bilayer film and pristine $Alq_3$ reference.

The spectra shown in the Fig. A-1 is from the experiment of the SGM beamline. However, same experiments on a new sample was also measured in the REIXS (Resonant Elastic and Inelastic X-ray Scattering) beamline at the CLS. The TEY spectra showed same result as SGM beamline, hence unusable for the further analysis.

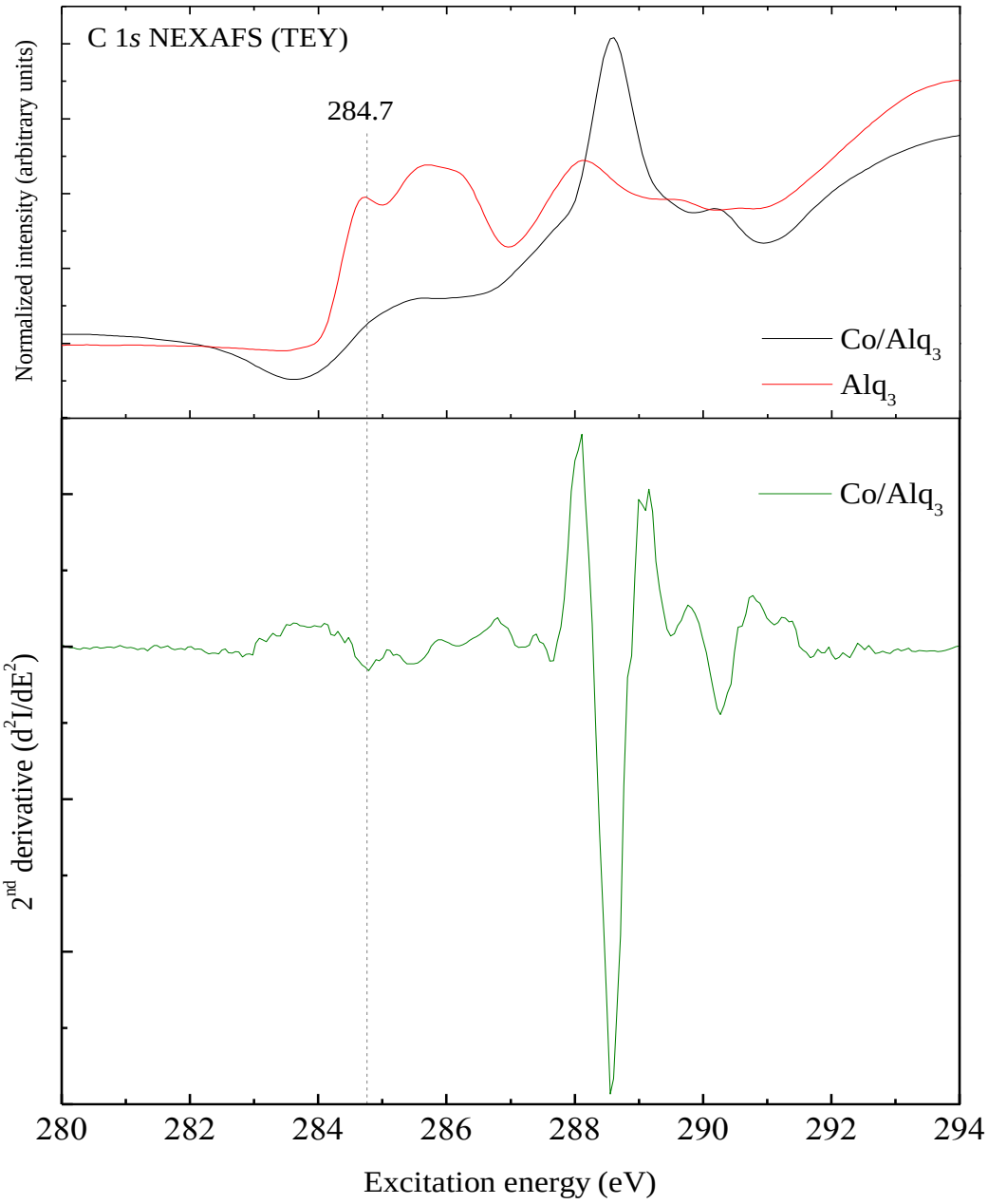


Figure A-2: C 1s TEY spectra of $Co/Alq_3$ bilayer film and pristine $Alq_3$ reference (upper panel) and the second derivative spectrum of the C 1*s* TEY of $Co/Alq_3$ (lower panel). There is the HOMO pick at 284.7eV in the C 1*s* TEY spectrum of $Co/Alq_3$ which is hidden because of the very low initial deep/intensity in the spectrum.

# REFERENCES


[1] H. C. Tong, C. Qian, L. Miloslavsky, S. Funada, X. Shi, F. Liu, and S. Dey, *J. Magn. Magn. Mater*. **209**, 56-60 (2000).

[2] P. D. Sparks and R. H. Silsbee, *Phys. Rev. B* **35**, 5198–5208 (1987).

[3] C. W. Tang and S. A. VanSlyke, *Appl. Phys. Lett.* **51**, 913 (1987).

[4] S. Pramanik and S. Bandyopadhyay, *Phys. Rev. B* **74**, 235329 (2006).

[5] W. Thomson, *Proc. R. Soc. London A*, **8**, pp. 546–550 (1856–1857).

[6] M. N. Baibich, J. M. Broto, A. Fert, F. Nguyen Van Dau, and F. Petroff, *Phys. Rev. Lett*. **61**, 2472-2475 (1988).

[7] G. Binasch, P. Grünberg, F. Saurenbach, and W. Zinn, *Phys. Rev. B* **39**, 4828-4830 (1989).

[8] M. Julliere, *Phys. Lett. A* **54**, 225–226 (1975).

[9] S. Ikeda, J. Hayakawa, Y. Ashizawa, Y. M. Lee1, K. Miura, H. Hasegawa, M. Tsunoda, F. Matsukura, and H. Ohno, *Appl. Phys. Lett.* **93**, 082508 (2008).

[10] V. A. Dediu, L. E. Hueso, I. Bergenti, and C. Taliani, *Nat. Mater.* **8**, 707-716 (2009).

[11] V. I. Krinichnyl, S. D. Chemerisov, and Y. S. Lebedev, *Phy. Rev. B* **55**, 16233-16244 (1997).

[12] V. Dediu, M. Murgia, F. C. Matacotta, C. Taliani, and S. Barbanera, *Solid State Commun*. **122**, 181-184 (2002).

[13] M. Bowen, M. Bibes, A. Barthélémy, J.-P. Contour, A. Anane, Y. Lemaître, and A. Fert, *Appl. Phys. Lett.* **82**, 233 (2003).

[14] Z. H. Xiong, D. Wu, Z. Valy Vardeny, and J. Shi, *Nature* **427**, 821 (2004).

[15] A. Riminucci, I. Bergenti, L. E. Hueso, M. Murgia, C. Taliani, Y. Zhan, F. Casoli, M. P. de Jong, and V. Dediu, arXiv:cond-mat/0701603 (2007).

[16] V. Dediu, L. E. Hueso, I. Bergenti, A. Riminucci, F. Borgatti, P. Graziosi, C. Newby, F. Casoli, M. P. De Jong, C. Taliani, and Y. Zhan, *Phys. Rev. B* **78**, 115203 (2008).

[17] T. S. Santos, J. S. Lee, P. Migdal, I. C. Lekshmi, B. Satpati, and J. S. Moodera, *Phys. Rev. Lett*. **98**, 016601 (2007).

[18] S. Majumdar, R. Laiho, P. Laukkanen, I.J.Väyrynen, H.S. Majumdar, and R. Österbacka, *Appl. Phys. Lett.* **89**, 122114 (2006).

[19] J. S. Jiang, J. E. Pearson, and S. D. Bader, *Phys. Rev. B* **77**, 035303 (2008).

[20] W. Brutting, S. Berleb, and A.G. Muckl, *Org. Electron.* **2**, 1 (2001).

[21] R. van Leeuwen, *Adv. Quantum Chem.* **43**, 25–94 (2003).

[22] S. Cottenier, *Density Functional Theory and the Family of (L)APW-methods: a step-by-step introduction* (Insti-tuut voor Kern-en Stralingsfysica, K. U. Leuven, Belgium) 2nd Edition, 2004.

[23] N. M. Harrison, *An Introduction to Density Functional Theory,* NATO Science Series III, Ed. Catlow and Kotomin, **187** (2003).

[24] W. Kohn, A. D. Becke, and R. G. Parr, *J. Phys. Chem.* **100**, 12974-12980 (1996).

[25] P. Hohenberg and W. Kohn, *Phys. Rev.* **136**, B864–B871 (1964).

[26] W. Kohn and L. J. Sham, *Phys. Rev.* **140**, A1133–A1138 (1965).

[27] S. Kümmel, L. Kronik, *Rev. Mod. Phys.* **80**, 3–60 (2008).

[28] S. J. Kang, Y. Yi, C. Y. Kim, C. N. Whang, T. A. Callcott, K. Krochak, A. Moewes, and G. S. Chang, *Appl. Phys. Lett.* **86**, 232103 (2005).

[29] J. Peter Guthrie, *J. Phys. Chem. A* **105**, 8495–8499 (2001).

[30] P. J. Stephens, F. J. Devlin, C. F. Chabalowski, and M. J. Frisch, *J. Phys. Chem.* **98**, 11623–11627 (1994).

[31] T. Regier, J. Krochak, T.K. Sham,Y.F. Hu, J. Thompson, R.I.R. Blyth. *Nucl. Instrum. Methods Phys. Res., Sect. A.* **582**, 93 (2007).

[32] J. J., Jia, T. A. Callcott, J. Yurkas, A. W. Ellis, F. J. Himpsel, M. G. Samant, J. Stöhr, D. L. Ederer, J. A. Carlisle, E. A. Hudson, L. J. Terminello, D.K. Shuh, R.C.C. Perera, *Rev. Sci. Instrum.* **66**, 1394 (1995).

[33] http://www.lightsource.ca/beamlines. *High Resolution Spherical Grating Monochromator (SGM) 11ID-1* (2014).

[34] http://www-als.lbl.gov/index.php/beamlines/beamlines-directory/115-801.html. *Beamline 8.0.1* (2014).

[35] H. Zeng, W. Huang, and J. Shi, *Chem. Commun*. **8**, 880-881 (2006).

[36] J. Stöhr, *NEXAFS Spectroscopy*, Springer-Verlag: Berlin (1996)